SYNOPSIS

Study of Structural, Optical and Magnetic Properties of Mn, Co, and Dy Doped Bismuth Ferrite Thin Films

1. Introduction

The term multiferroics have been coined to describe materials in which two or more ferroic orders coexist in a single phase, out of the four primary ferroic properties- ferroelectricity, ferromagnetism, ferroelasticity, and ferrotoroidicity [1]. The ferroic materials are one in which the spontaneous magnetization (Ms) can be reoriented by the external magnetic field (H); spontaneous polarization (Ps) can be reoriented by the external electric field (E), and the spontaneous deformation (ε_s) can be reoriented by external stress (σ). Among the multiferroic, magnetoelectric (ME) multiferroics, a subset of multiferroic materials, are very important materials in which electrical polarization can be induced by applying a magnetic field, and magnetization can be induced by applying an electric field and vice versa. The magnetoelectric multiferroics find applications for the designing of novel spintronic devices such as tunneling magnetoresistance (TMR) sensors, spin valves with electric field tunable functions [2], and multistate memory devices in which data are written electrically and read magnetically [3].

In 1888, Rontgen observed that a moving dielectric body placed in a magnetic field became magnetized or vice-versa [4]. Moreover, these are not the intrinsic effects of materials. In 1894, Curie envisaged the probability of magnetoelectric effect in some crystals [5] using crystal symmetry considerations which were subsequently coined by Debye as "magnetoelectric effect" [6]. Cr_2O_3 was the first material in which the magnetoelectric effect was successfully observed with a magnetoelectric coupling coefficient is 4.13 ps/m [7]. In the past, more than 100 compounds have been discovered exhibiting the magnetoelectric effect and remain key materials for the highly fascinating multiferroic research [8]. Unfortunately, in single-phase compounds, the magnetoelectric effect is usually too weak to be practically applicable.

One way to substantially improve the coupling between electric and magnetic orders is to utilize strong internal electromagnetic fields in materials with large magnetic and electric susceptibilities. It is well known that the largest magnetic and electric susceptibilities

are found in ferromagnetic/ferroelectric materials. Ferroelectrics with ferromagnetism, i.e., electromagnets could be utilized for an improved magneto-electric effect [9]. Consequently, the term multiferroics were coined by Schmid, for those compounds which simultaneously possess two or more primary ferroic orders in a single phase (ferroelectricity, ferromagnetism, and ferroelasticity) [10].

It has proved difficult to discover new intrinsic multiferroic materials because the mechanisms driving ferroelectricity and ferromagnetism are generally incompatible. Ferroelectricity is usually generated by transition metal compounds with empty d-orbits (d^0). For example, in $BaTiO_3$ the ferroelectricity is caused by the cooperative shifting of the Ti^{4+} cation along the [111] direction; this off-centering is stabilized by covalent bonding between the oxygen 2p orbits and the empty d-orbits of Ti^{4+} [11]. On the other hand, ferromagnetism usually requires a transition metal with partially filled d-orbits. Consequently, a different approach is required to combine these two properties.

For the integration of ferroelectricity and ferromagnetism, the conceptually simplest strategy is to synthesize materials with discrete functional units. Normally, we aid the non-centrosymmetric units, which provide a strong dielectric response and ferroelectricity, together with magnetic ion units. An alternative way is attributed to ABO_3 type perovskite oxides, wherein A-sites are usually occupied by cat-ions of $6s^2$ valence electron configuration, such as Bi^{3+}, Pb^{2+}, which favor the stability of ferroelectrically distorted structures, and B-site, are occupied by magnetic ions contributing to magnetism. This strategy evades the mutually exclusive ferroelectricity and magnetism at the same site because; ferroelectricity originates from A-site ions and magnetism generated from B-site magnetic ions. It provides an effective combination of the electric and magnetic orders along with a mutual control between them. However, in this type of multiferroics, the coupling between ferroelectric and magnetic ordering is very weak due to their different source of origin.

The A-site in the ABO_3 perovskite structure is always occupied by the ions with $6s^2$ electrons such as Bi^{3+} and Pb^{2+}. It allows magnetic transition metal ions to occupy B-site in the ABO_3 structure so that the mutually exclusive condition to induce both magnetism and ferroelectricity is partially relaxed. The Bismuth Ferrite ($BiFeO_3$) is a well-known example for this class of materials, where A-site ions via the lone pair mechanism led to the ferroelectricity and B-site ions produced magnetism. In $BiFeO_3$ the shifting of Bi-ions from centrosymmetric positions relative to surrounding oxygen ions induced ferroelectricity and

unpaired magnetic spins of Fe-ions provide magnetism. Hence, single-phase multiferroics $BiFeO_3$ (BFO) is the widely investigated material.

In bulk form material, BFO has been known to be an antiferromagnetic-ferroelectric multiferroic material [12, 13]. It has antiferromagnetic Neel temperature T_N~643 K and ferroelectric Curie temperature T_C~1103 K. BFO possesses distorted rhombohedral perovskite structure with R3c space group [14, 15]. The Fe magnetic moments are arranged in a ferromagnetic manner within the pseudocubic (111) plane, while connected antiferromagnetically between adjacent planes. Such a type of magnetic ordering of Fe moments is known as G-type antiferromagnetic ordering. The observation of a macroscopic magnetization (i.e., weak ferromagnetism) is allowed due to symmetry-driven canting of the antiferromagnetic sublattices, if Fe spins are aligned perpendicular to [111] axis [16, 17]. However, the observation of macroscopic magnetization and the linear magnetoelectric effect is prohibited due to a superimposed spiral spin structure in which the antiferromagnetic axis rotates through the crystal with an incommensurate long-wavelength period ~62 nm [18, 19].

Moreover, the synthesis of the BFO single phase is complicated, on one hand, by the high probability of the formation of impurity phases and, on the other hand, by the strong dependence of the physical properties on the oxygen stoichiometry and crystal perfection. High leakage current, as well as the presence of magnetic moments in the crystal, is compulsory for the practical application of BFO; therefore, particular interest has been paid for improving the dielectric properties, suppression of antiferromagnetic cycloid spiral spin order, and ensuring the optical behavior in the visible range of BFO. Substitution of foreign elements might be an effective way to enhance the macroscopic magnetic moment because chemical doping can change electrical conductivity along with improvement in magnetic behavior via changing the ligand field of Fe-ions.

This is because a slight change in atomic composition can produce large distortion within perovskite unit cells that might have dramatic impacts on the properties of the material such as structural evolution, optical, and magnetic properties. Within the last decade, enormous growth has been made in the understanding of BFO.

2. Aim and Scope of the Present Work:

The main aim of the present work is

1. To synthesize and study the properties of BFO thin films using a simple low-cost sol-gel spin-coating method directly on glass and p-silicon substrates.

2. To study the effects of transition metal and rare earth metal ion doping on the structural, morphological, optical, and magnetic properties of these sol-gel spin-coated BFO thin films. Since transition metal and rare earth, doping is envisaged as the important way to improve the multiferroic properties of BFO thin films, and these studies are currently under intense investigation. The transition metal ions used for the doping were Manganese (Mn) and Cobalt (Co), which substitute for the Fe (B-site) in $BiFeO_3$. Dysprosium (Dy) was the rare earth metal ion used in the present study, which substitutes for Bi in $BiFeO_3$.
3. Powder XRD, FESEM, and AFM were the method intended to use for the structural and morphological studies, respectively. UV-visible spectroscopy, FTIR spectroscopy, and Raman spectroscopy were indented for optical studies of the BFO thin films. The M-H characterization was utilized to study the magnetic properties of the BFO thin films.
4. Interpretation of the properties of the synthesized BFO thin films based on the experimental results.

3. Materials Synthesis and Characterization

Synthesis process

1) The synthesis of undoped and doped BFO with transition metals (Mn, Co) thin films on glass and p-Si substrates. The sequence of spin coating followed by the annealing process was repeated to obtain the films with the required thickness and crystalline form nanostructured thin films. The effect of annealing under ambient air and argon atmosphere was tried.

2) The fabrication of undoped and doped BFO with rare earth metals (Dy) thin films on glass and p-Si substrates using the sol-gel spin coating process. The spin-coated films were annealed argon gas environment.

Characterization

The techniques utilized for structural, morphological, optical, and magnetic characterization are as follows:

1) RigakuMiniflex-600 X-ray diffractometer (XRD) is used to investigate the composition, orientation, dislocation density and strain, crystal structure, crystallite size, and crystal lattice characteristics of BFO thin films.

2) ULTRA 55 Zeiss Field Emission Scanning Electron Microscopy (FESEM) and Nanosurf easy scan2 Atomic Force Microscopy (AFM) utilized for surface morphology and topographic investigations. Energy-dispersive X-ray spectroscopy (EDS) attachment in the FESEM system was used for the determination of the chemical composition of the grown thin films.

3) Shimadzu Ultraviolet-Visible-1800 spectrophotometer provides information on thin-film absorption and transmission. From the measure optical absorption spectra, the optical bandgap of the grown films was estimated.

4) Fourier transform infrared (FTIR) spectra were recorded using Shimadzu IR Prestige 21 FTIR spectrometer with ATR setup.

5) Raman spectra of BFO thin films were studied using the Ventana-532-Raman spectroscopy.

6) The low and room temperature M-H curve of undoped and Mn-doped $BiFeO_3$ thin films was measured by using Quantum Designs/MPMS 3-111-SQUID magnetometer.

4. Thesis organization

The thesis is divided into six chapters, the contents of which are as follows:

4.1 Chapter-1: Introduction

This chapter provides a brief introduction to the area of multiferroics and multiferroic BFO thin-film materials. A brief account has been given on the BFO multiferroic phenomenon that provides a summary of the theoretical, conceptual, experimental, and material aspects. We have set our objective for this study based on the literature survey. Multiferroics are the materials that exhibit simultaneously at least two of the ferroic ordering among the ferroelectricity, ferromagnetism, and ferroelasticity [20]. The coupling of these order parameters provides multiferroic materials novel properties which make them promising candidates for novel multifunctional devices such as spintronics, transducers, data-storage media, etc. [21]. Among the multiferroics, magnetoelectric multiferroics are the

materials with ferroelectric and ferromagnetic coupling in a single phase. The study of the ME multiferroic materials attracted greater interest due to their potential applications [22]. Among the ME multiferroic materials, Bismuth ferrite ($BiFeO_3$) is the most promising material because it shows both ferroelectric and antiferromagnetic behavior above room temperature; it has a ferroelectric Curie temperature of about 1103 K and G-type antiferromagnetic Neel temperatures of about 643 K [23, 24]. The bulk $BiFeO_3$ material exhibits a rhombohedral distorted perovskite (ABO_3) crystal structure with an R3c space group at room temperature. The existence of Bi 6s lone-pair stereochemical electrons is accountable for the off-center shift of the Bi atom from the central to the non-centrosymmetric structure, and hence the ferroelectricity. The ferromagnetism originates from the partially filled 3d orbital of the Fe metal cat-ions [25]. However, in bulk $BiFeO_3$ the modulation of the G-type antiferromagnetic structure to a long-range spin cycloid of a period of about 62 nm results in weakening of the ferromagnetism [26]. Also, the volatilization of Bi during the synthesis leads to secondary phase formation (Bi_2O_3/Fe_2O_3/$Bi_2Fe_4O_9$/$Bi_{25}FeO_{40}$) as well as non-stoichiometry in bulk $BiFeO_3$ which is detrimental for the observation of ferroelectricity [27]. Due to non-stoichiometry, $BiFeO_3$ in the bulk phase shows a large leakage current which makes it difficult to measure accurately the ferroelectric properties in the same material. The above issues limit the usage of bulk $BiFeO_3$ in the fabrication of functional devices [28]. In thin-film forms of $BiFeO_3$, the spin cycloid structure was reported to be suppressed [24]. The electrical property of $BiFeO_3$ thin films was found to be sensitive to process conditions and impurities. Recently, it was discovered that the multiferroic properties of $BiFeO_3$ thin films can be highly enhanced by substituting with rare-earth (La, Nd, Gd, or Sm) or 3d-transition elements (Mn, Co, Cu, Zn, Mg, or Cr) either at A-site or B-site or A, B-sites [29, 30, 31, 32].

4.2. Chapter-2: Experimental Method and Characterizations

This chapter gives a brief description of the experimental methods used in the present investigation. The synthesis method, the sol-gel spin coating method was employed in the present study for the synthesis of $BiFeO_3$ thin films has been briefly described at the beginning of the chapter. A brief description of the characterization techniques employed in the present study is given in the chapter. The powder X-ray diffraction (XRD), Field emission secondary electron microscopy (FESEM), Energy-dispersive X-ray spectroscopy (EDS), atomic force microscopy (AFM), UV-Visible, FTIR, and Raman spectroscopy are used to study the structural, morphological, elemental, and optical properties of the synthesized thin

films. The low and room-temperature magnetic properties (M-H curve) of thin films were measured by using the Quantum Designs/MPMS 3-111-SQUID magnetometer.

4.3 Chapter-3: Preparation and characterization of $BiFeO_3$ and Mn-substituted $BiFeO_3$ thin films on glass and p-Si substrates

In the present chapter, the synthesis and characterization aspects of undoped bismuth ferrite ($BiFeO_3$) and manganese (Mn)-doped $BiFeO_3$ ($BiFe_{1-x}Mn_xO_3$ for $0.0 \leq x \leq 0.06$) multiferroic thin films are discussed. The undoped bismuth ferrite ($BiFeO_3$) and manganese (Mn)-doped $BiFeO_3$ ($BiFe_{1-x}Mn_xO_3$ for $0.0 \leq x \leq 0.06$) multiferroic thin films were deposited on glass and p-Si (100) substrates through the sol-gel spin-coating method.

The synthesized undoped and Mn-doped BFO thin films were characterized by XRD, FESEM, and AFM, UV–Visible absorption spectroscopy, FTIR, Raman spectroscopy, and MPMS SQUID Quantum Designs/MPMS 3-111device measurements.

4.3.1 Results and Discussion

4.3.1.1 Undoped and Mn–Doped BFO Thin Films on Glass Substrates

Fig. 3.1 shows the XRD patterns of the $BiFeO_3$ and $BiFe_{1-x}Mn_xO_3$ thin films grown on glass substrates. The XRD patterns match with the JCPDS file No. 71-2494 of the rhombohedral distorted structure of $BiFeO_3$, which belongs to the R3c space group. All the samples show additional peaks at 2θ value of 27^o, 29^o, and 35^o related to the impurity phase $Bi_2Fe_4O_9$ due to the metastable structure of $BiFeO_3$ in air and the volatility of bismuth oxide. The appearance of (104) and (110) twin peaks is an indication of the distorted rhombohedral structure of $BiFeO_3$. By Mn doping and increasing the Mn concentration from x= 0.02 to x= 0.06, the (104) shifts towards a higher angle. At x=0.06, the (104) and(110) peaks merge to form a single broad peak. This suggests that the rhombohedral distorted structure of $BiFeO_3$ thin film transforms towards an orthorhombic structure after the substitution of Fe with Mn. The average crystallite size of the grown thin films is determined using Scherrer's formula. The lattice strain (η), and the value of dislocation density was calculated. The average crystallite size of $BiFeO_3$ was found to decrease with an increase in Mn substitution due to the smaller ionic radii of Mn.

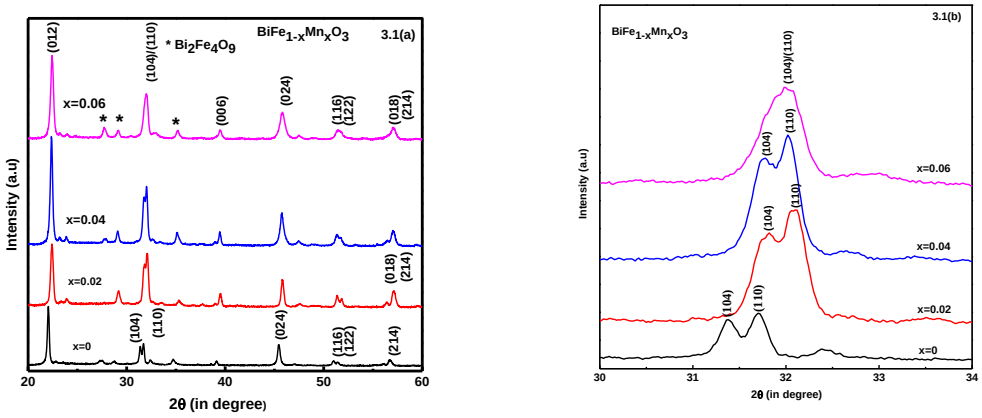

Fig. 3.1(a) and (b): XRD pattern and magnified XRD patterns of $BiFeO_3$ and $BiFe_{1-x}Mn_xO_3$ thin films in the vicinity of $2\theta = 32°$ with (a) x=0 (b) x=0.02 (c) x=0.04 and (d) x=0.06.

Fig. 3.2(a–d) shows the FESEM images of the $BiFeO_3$ and $BiFe_{1-x}Mn_xO_3$ thin films. Fig. 3.2(e) shows the FESEM cross-sectional image of the $BiFe_{1-x}Mn_xO_3$ thin film that indicates that the thickness of the grown thin film is approximately 1.2 μm. The grain size of $BiFe_{1-x}Mn_xO_3$ has been observed to be smaller than the $BiFeO_3$ thin film. The reduction in grain size might be attributed to an increase in lattice strain in the $BiFe_{1-x}Mn_xO_3$ nanocrystal thin films.

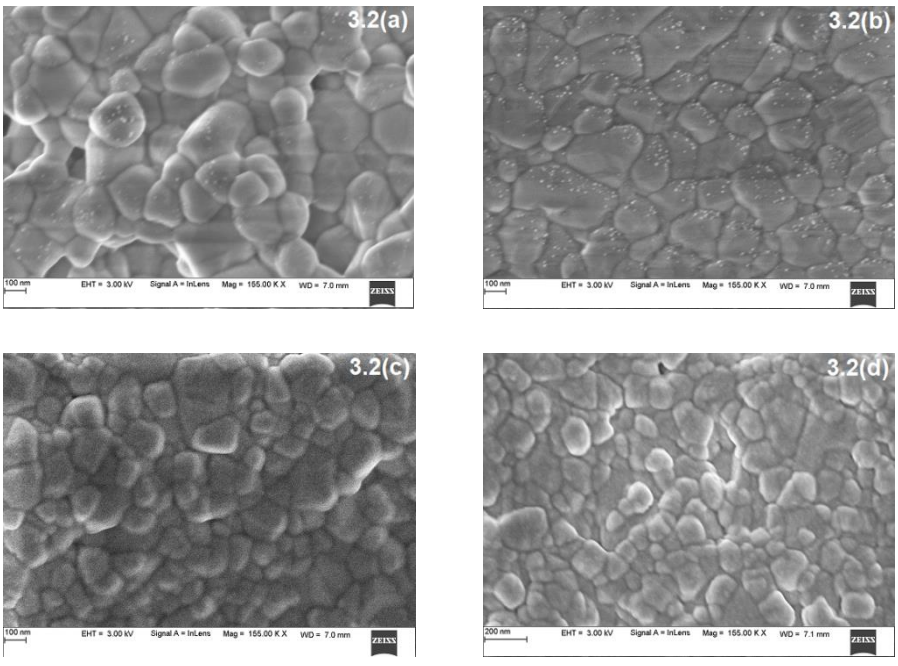

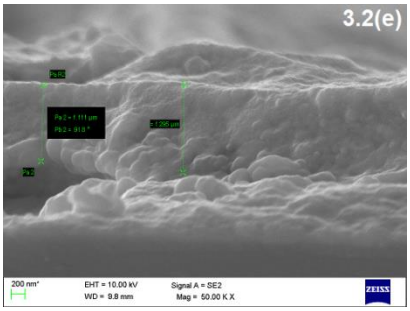

Fig. 3.2(a-d): Surface morphology of BFO and $BiFe_{1-x}Mn_xO_3$ thin films with (a) x=0 (b) x=0.02 (c) x=0.04 and (d) x=0.06 and **3.2(e):** Cross-sectional image of $BiFe_{1-x}Mn_xO_3$ thin film.

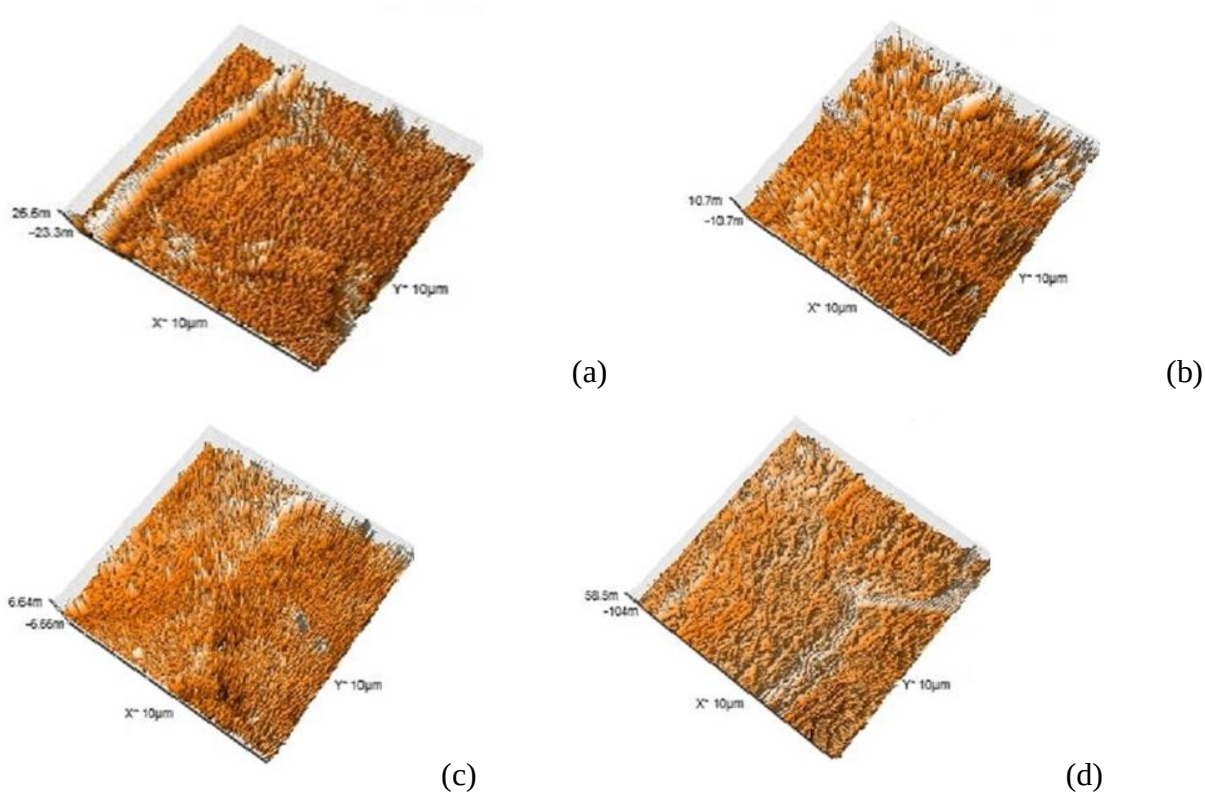

Fig. 3.3(a-d): Surface topography images of $BiFeO_3$ and $BiFe_{1-x}Mn_xO_3$ thin films with (a) x=0 (b) x=0.02 (c) x=0.04 and (d) x=0.06.

Fig. 3.3(a-d) shows the AFM surface topography images of $BiFeO_3$ and $BiFe_{1-x}Mn_xO_3$ thin films. The average and root-mean-square (RMS) value surface area roughness for $BiFeO_3$ and $BiFe_{1-x}Mn_xO_3$ thin films were measured and found to decrease with the increase in Mn substitution.

The UV-visible absorption spectra of $BiFeO_3$ and $BiFe_{1-x}Mn_xO_3$ thin films are shown in Fig. 3.4 (a). The energy bandgap of the thin film materials was calculated from the optical

absorption using Tauc's plot $(\alpha h\nu)^2$ versus hν as in shown Fig. 3.4(b). The band gap was found to decrease (redshift) with the increase in Mn concentration. The observed energy bandgap red-shift may be associated with the transformation of rhombohedral distorted structure towards orthorhombic structure due to the rearrangement of molecular orbitals and distortion induced in the Fe-O_6 octahedral.

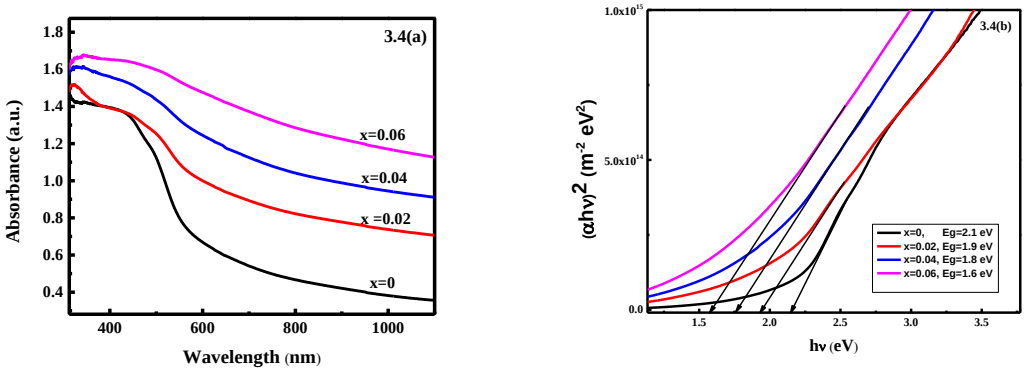

Fig. 3.4(a): UV-Vis absorption spectra, **3.4(b):** Plot of $(\alpha h\nu)^2$ vs hν of BFO and $BiFe_{1-x}Mn_xO_3$ thin films.

The FTIR spectra of $BiFeO_3$ and $BiFe_{1-x}Mn_xO_3$ thin films are shown in Fig. 3.5. The formation of the perovskite structured $BiFeO_3$ thin film is confirmed by the presence of a metal-oxide absorption band in the region of 480 cm^{-1} to 660 cm^{-1} [28, 29]. The absorption bands around 800 cm^{-1} and 1320 cm^{-1} correspond to the presence of trace amounts of NO^{3-}. The absorption band at around 980 cm^{-1} may be due to vibrations of the C-H bond.

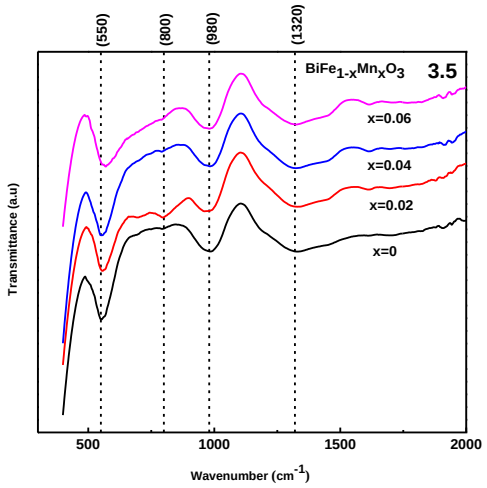

Figure 3.5: FTIR spectra of BFO and $BiFe_{1-x}Mn_xO_3$ thin films.

Fig. 3.6 shows the Raman spectra of the $BiFeO_3$ and $BiFe_{1-x}Mn_xO_3$ thin films. For the R3c space group, the theoretical analysis predicts 13 Raman active phonon modes at the Γ point, $\Gamma = 4A_1+9E$. The observed Raman modes are in good agreement with the rhombohedral distorted R3c perovskite structure.

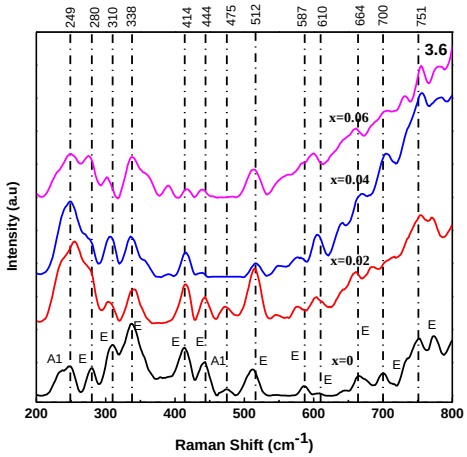

Fig. 3.6: Raman spectra of BFO and $BiFe_{1-x}Mn_xO_3$ thin films with (a) x=0 (b) x=0.02 (c) x=0.04 and (d) x=0.06.

M-H curves of $BiFe_{1-x}Mn_xO_3$ thin films with x=0, 0.02, 0.04, and 0.06 measured at low 10 K and room temperature 300 K with an applied magnetic field up to 70 kOe and are shown in Fig. 3.7, 3.8, 3.9, and 3.10, respectively. The room temperature M-H curve in all the films shows hysteresis loops with high field ferromagnetic saturation with narrow loop width along with a strong diamagnetic contribution from the glass substrate superimposed at high magnetic fields. The substrate diamagnetic contribution in the room temperature M-H data has been excluded using a linear fit to the measured M-H data. The slope of the linear portion of the high magnetic field M-H plot, where the ferromagnetic contribution is saturated, has been used to set the slope of the linear fit to the measured data. The substrate diamagnetic contribution excluded M-H plots indicate the characteristic weak ferromagnetism of the $BiFe_{1-x}Mn_xO_3$ thin films at room temperature. The raw data M-H plots measured at 300 K are shown as an inset to the M-H plots of the respective, samples as shown in Fig. 3.7, 3.8, 3.9, and 3.10. The nanostructured thin films may be leading to suppression of the long-range (62 nm) space modulated spin cycloid structure and this may be responsible for the observed weak ferromagnetism in the $BiFe_{1-x}Mn_xO_3$ thin films at room temperature. The M-H loops of all the $BiFe_{1-x}Mn_xO_3$ thin films measured at 10 K indicate the superparamagnetic behavior with a large increase in magnetization in comparison with room temperature magnetization.

The literature review shows that ferromagnetic and ferrimagnetic materials nanoparticles with sizes less than 50 nm, which are single-domain nanoparticles, show superparamagnetism.

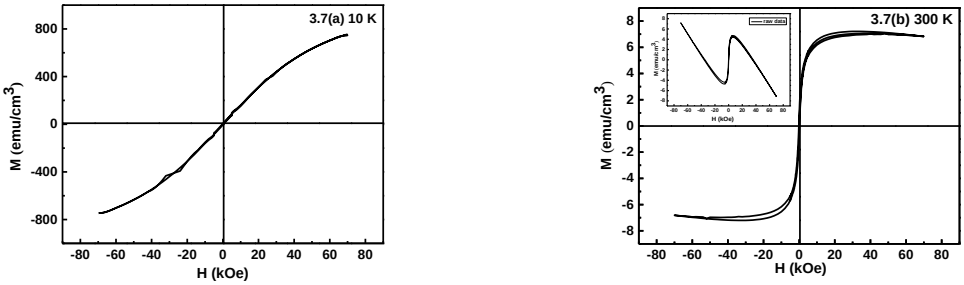

Fig. 3.7(a) and (b): Low and room-temperature M-H hysteresis loops of BFO thin film with x=0.

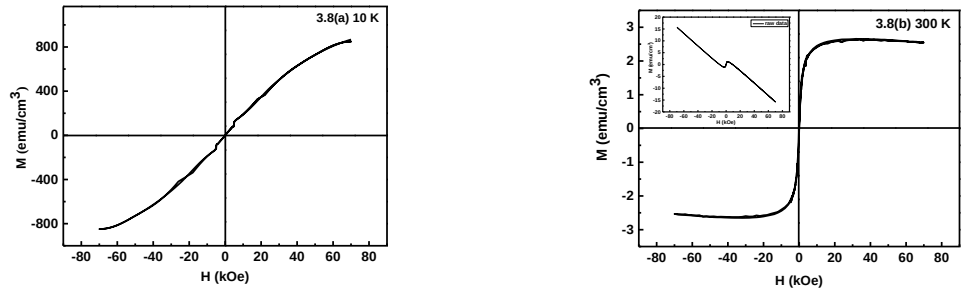

Fig. 3.8(a) and (b): Low and room-temperature M-H hysteresis loops of BFO thin film with x=0.02.

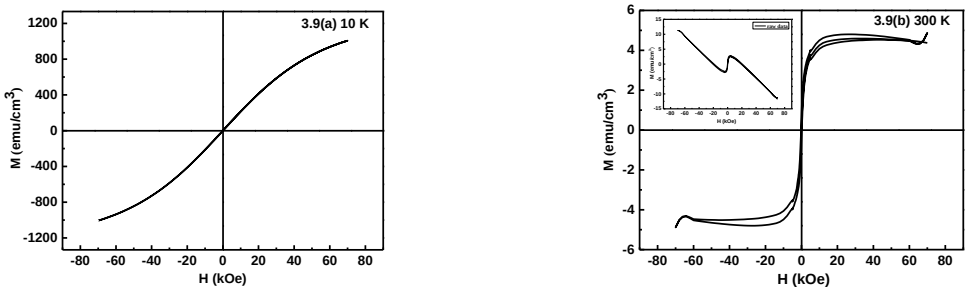

Fig. 3.9(a) and (b): Low and room-temperature M-H hysteresis loops of BFO thin film with x=0.04.

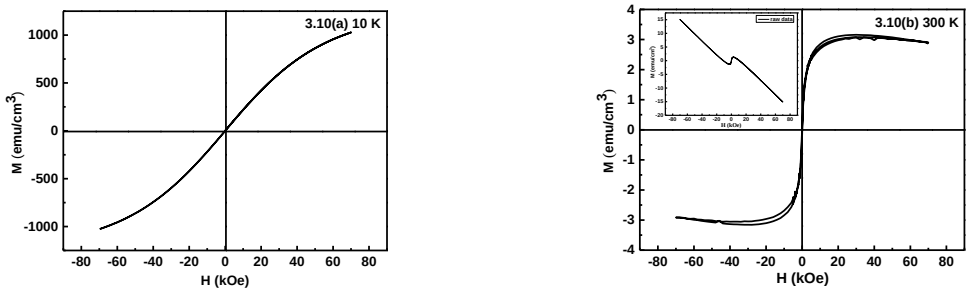

Fig. 3.10(a) and (b): Low and room-temperature M-H hysteresis loops of BFO thin film with x=0.06.

4.3.1.2 Undoped and Mn–Doped BFO Thin Films on p-Si Substrates

Fig. 3.11 shows the XRD patterns of BFO and $BiFe_{1-x}Mn_xO_3$ thin films. The XRD results indicate that BFO thin film has distorted perovskite rhombohedral structure as found by matching with the JCPDS file # 71-2494. The characteristic (104) and (110) twin peaks indicate the distorted perovskite rhombohedral structure merging into a single peak for x=0.06. This result suggests that, due to lattice distortion, the rhombohedral structure of BFO tends to change with an increase in Mn content. The average crystallite size of $BiFeO_3$ thin films was found to decrease with an increase in Mn substitution due to the smaller ionic radii of Mn.

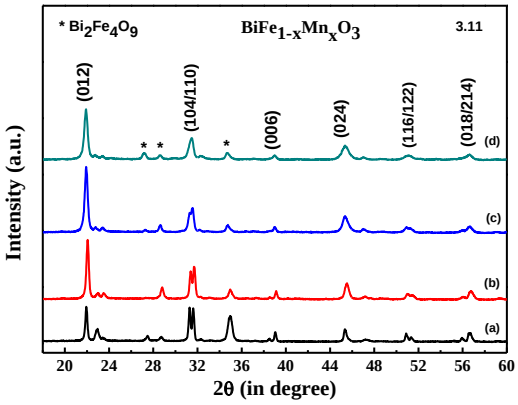

Fig. 3.11: XRD patterns of $BiFe_{1-x}Mn_xO_3$ thin films with (a) x=0, (b) x=0.02, (c) x=0.04, and (d) x=0.06.

Fig. 3.12(a–d) shows the FESEM images of the grown thin films. The BFO thin film show well-distinguished grains with a large size of the order of 211 nm in diameter. The grain size decreased as the Mn doping concentration was increased and the films appear clearly and more densely packed.

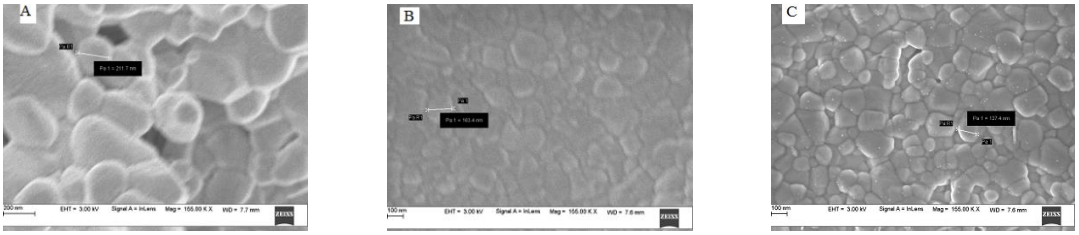

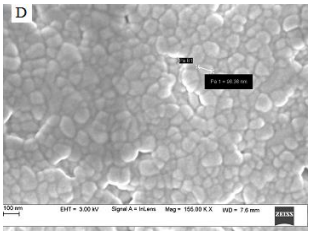

Fig. 3.12(a-d): Surface morphology of BFO and $BiFe_{1-x}Mn_xO_3$ thin films with (a) x=0 (b) x=0.02 (c) x=0.04 and (d) x=0.06.

Fig. 3.13(a-d) shows the AFM images of the grown films; an increase in Mn doping leads to the growth of films with smooth surface topography, the size and number of hills are reduced with an increase in Mn doping. The average, root-mean-square (RMS) values of line and area surface smoothness for the BFO and BFMO thin films were obtained from AFM studies and found that it has decreased with an increase in Mn doping.

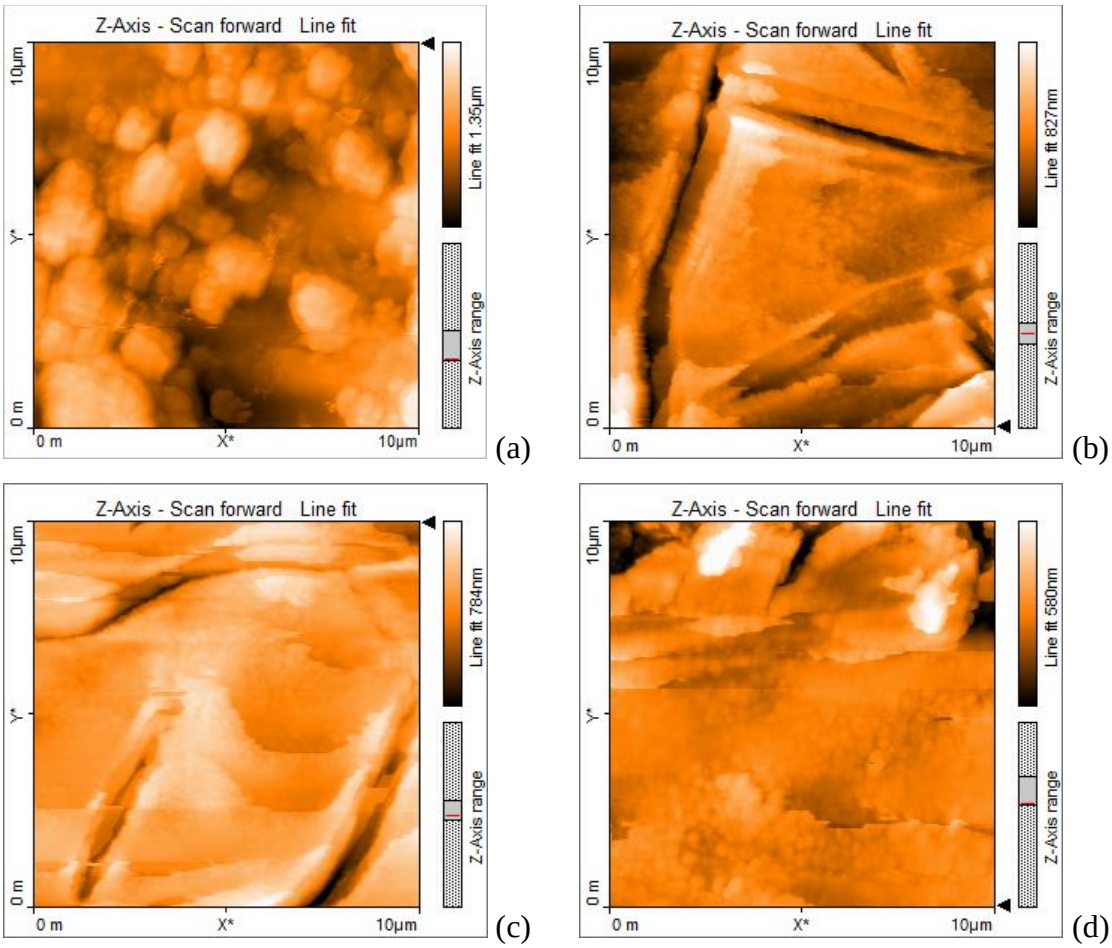

Fig. 3.13(a-d): Surface topography images of $BiFe_{1-x}Mn_xO_3$ thin films with (a) x=0 (b) x=0.02 (c) x=0.04 and (d) x=0.06.

Magnetization (M-H) loops for $BiFe_{1-x}Mn_xO_3$ thin films with x=0, 0.02, 0.04, and 0.06 were measured at 10 K and room temperature with an applied magnetic field up to 70 kOe and are shown in Fig. 3.14–3.17. The M-H curves measured at room temperature show the ferromagnetic behavior in all the samples. The 10 K M-H curves of the Mn-doped $BiFe_{1-x}Mn_xO_3$ thin films exhibit ferromagnetic behavior. The M-H curve of undoped BFO indicates superparamagnetism.

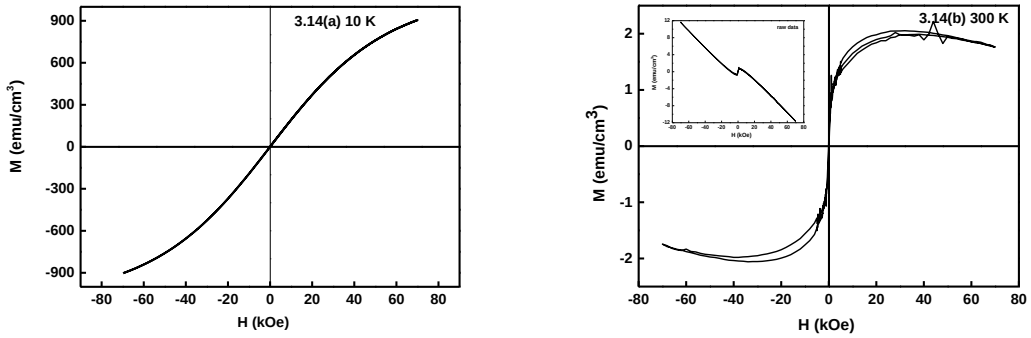

Fig. 3.14(a) and (b): Low and room-temperature M-H hysteresis loops of BFO thin film with x=0.

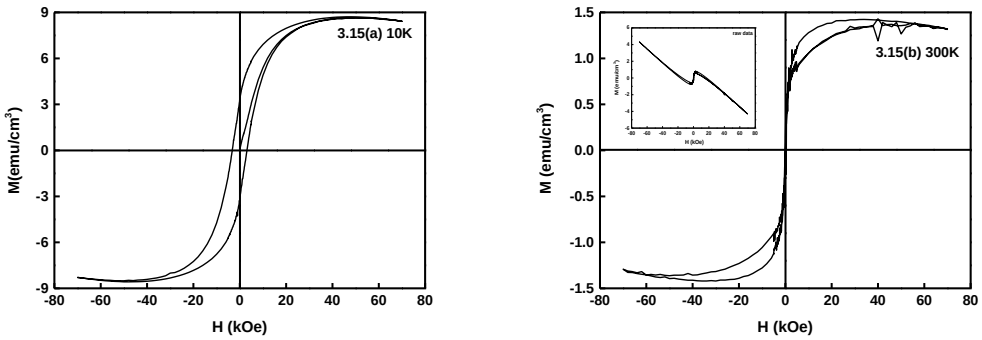

Fig. 3.15(a) and (b): Low and room-temperature M-H hysteresis loops of BFO thin film with x=0.02.

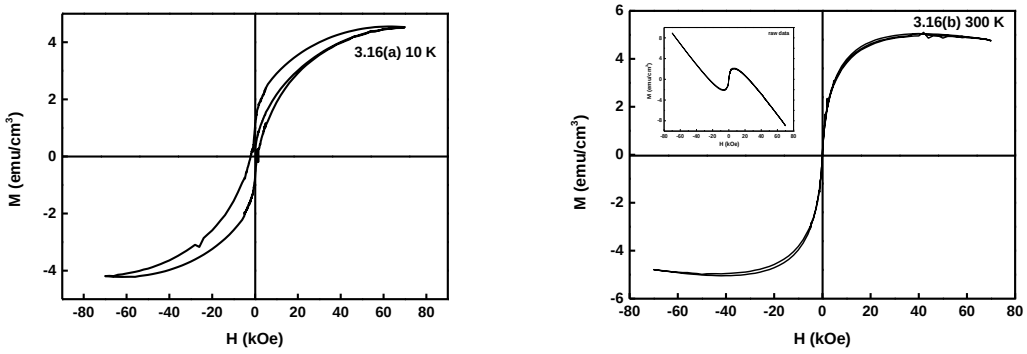

Fig. 3.16(a) and (b): Low and room-temperature M-H hysteresis loops of BFO thin film with x=0.04.

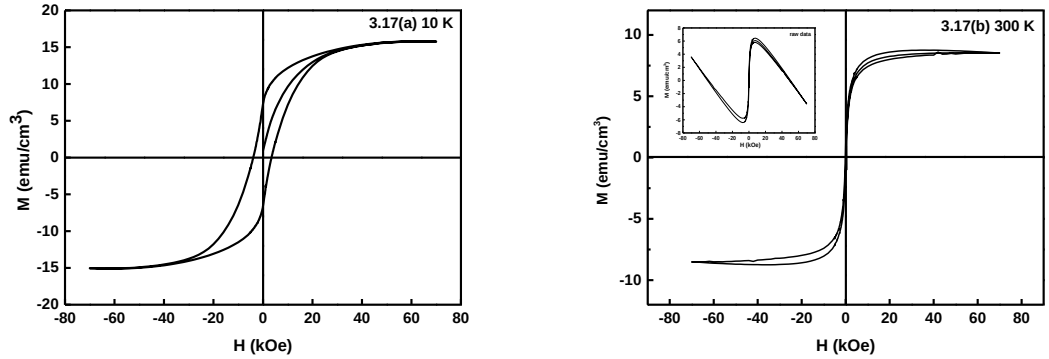

Fig. 3.17(a) and (b): Low and room-temperature M-H hysteresis loops of BFO thin film with x=0.06.

4.4 Chapter 4: Growth and Characterization of Undoped and Cobalt doped $BiFeO_3$ Thin Films Coated on Glass and p-Si Substrates

As discussed earlier, a noticeable impact has been made to get both strong ME multiferroic effects in perovskite $BiFeO_3$ through A-site and/or B-site doping. Most of the studies concentrated on the Fe-site ion substitution with magnetic ions to increase the ferromagnetic property. In this study, we have investigated the effect of cobalt substitution on the structural and optical properties of $BiFeO_3$ thin films.

Undoped and Co-doped BFO thin films were deposited on glass and p-Si substrates by the sol-gel spin coating method. Iron nitrate monohydrate [$Fe(NO_3)_3.9H_2O$], bismuth nitrate pentahydrate [$Bi(NO_3)_3.5H_2O$], and cobalt acetate tetrahydrate [$Co(OOCH_3)_2.4H_2O$]

were used as starting materials. 2-methoxyethanol and acetic anhydride in a 3:1 ratio were used as solvents.

4.4.3 Results and Discussion

4.4.3.1 Undoped and Cobalt-Doped BFO Thin Films on Glass Substrates

Fig. 4.1 shows the XRD pattern of the $BiFeO_3$ and $BiFe_{1-x}Co_xO_3$ nanostructured thin films grown on glass substrates. The XRD patterns of the $BiFeO_3$ nanostructured thin films were compared with the JCPDS File No: 71-2494. The entire samples exhibit distorted polycrystalline rhombohedral perovskite crystal structure with the R3c space group. The synthesized $BiFeO_3$ and $BiFe_{1-x}Co_xO_3$ samples exhibited a few desirable secondary phases of $Bi_2Fe_4O_9$ (Marked with $*$). However, the Co-doing into the $BiFeO_3$ leads slight shift in the peak position at the 2θ values of 22.5° (corresponding to (100) plane) and 32.0° (corresponding to (104/110) plane) toward the higher angle. The average crystallite size of the grown $BiFeO_3$ and $BiFe_{1-x}Co_xO_3$ nanostructured thin films were determined by using Scherrer's formula and found to increase with the increase in Co ion concentration, which may be due to the slightly larger ionic radii (1.88 Å) of Co^{2+} compared to the ionic radii of Fe^{2+} (1.90 Å). The lattice strain (ε) and dislocation density (δ) were estimated.

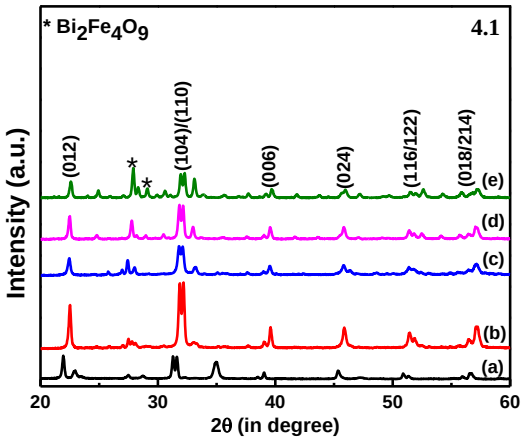

Fig. 4.1: XRD patterns of $BiFeO_3$ and $BiFe_{1-x}Co_xO_3$ nanostructured thin films with (a) x=0 (b) x=0.02 (c) x=0.04 (d) x=0.06, and (e) x=0.08.

Fig. 4.2(a-e) shows the FESEM images of $BiFeO_3$ and $BiFe_{1-x}Co_xO_3$ nanostructured thin films. The FESEM images indicate the increase in the grain size with an increase in Co doping in $BiFeO_3$ thin films. The larger grain size and dense nanostructure may result in

better ferromagnetic properties. Fig. 4.3 shows the cross-sectional FESEM image of the $BiFe_{1-x}Co_xO_3$ nanostructured thin film, which indicates that the thickness of the grown film is around 775 nm. Fig. 4.4(a-e) shows EDX spectra of the grown $BiFeO_3$ and $BiFe_{1-x}Co_xO_3$ nanostructured thin films. The EDX studies confirm the elemental compositions of the $BiFeO_3$ and $BiFe_{1-x}Co_xO_3$ nanostructured thin films and estimate.

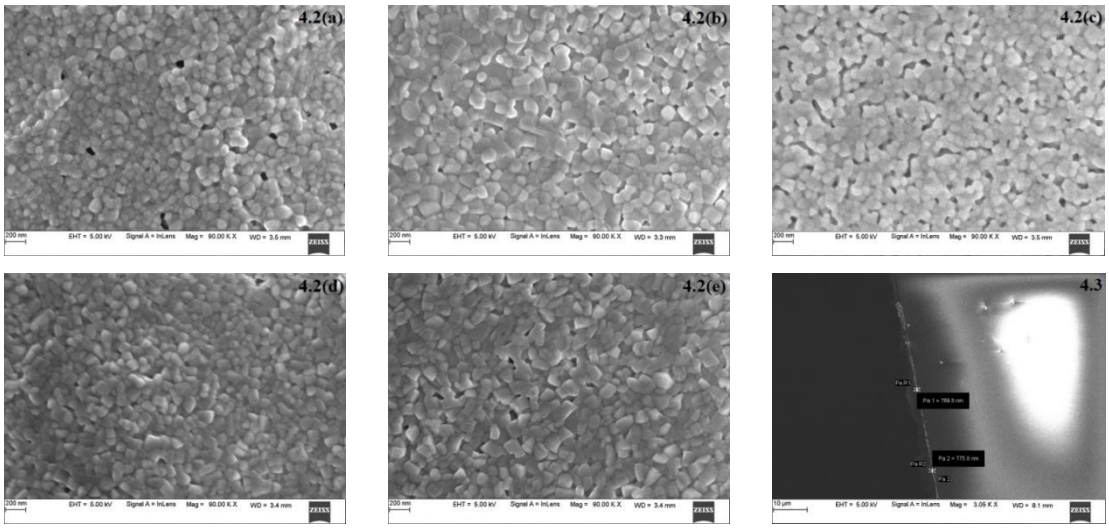

Fig. 4.2(a-e): (a) x=0, (b) x=0.02, (c) x=0.04, (d) x=0.06 and (e) x=0.08 shows the surface morphology of $BiFeO_3$ and $BiFe_{1-x}Co_xO_3$ nanostructured thin films.

Fig. 4.3: The cross-sectional image of $BiFe_{1-x}Co_xO_3$ nanostructured thin film.

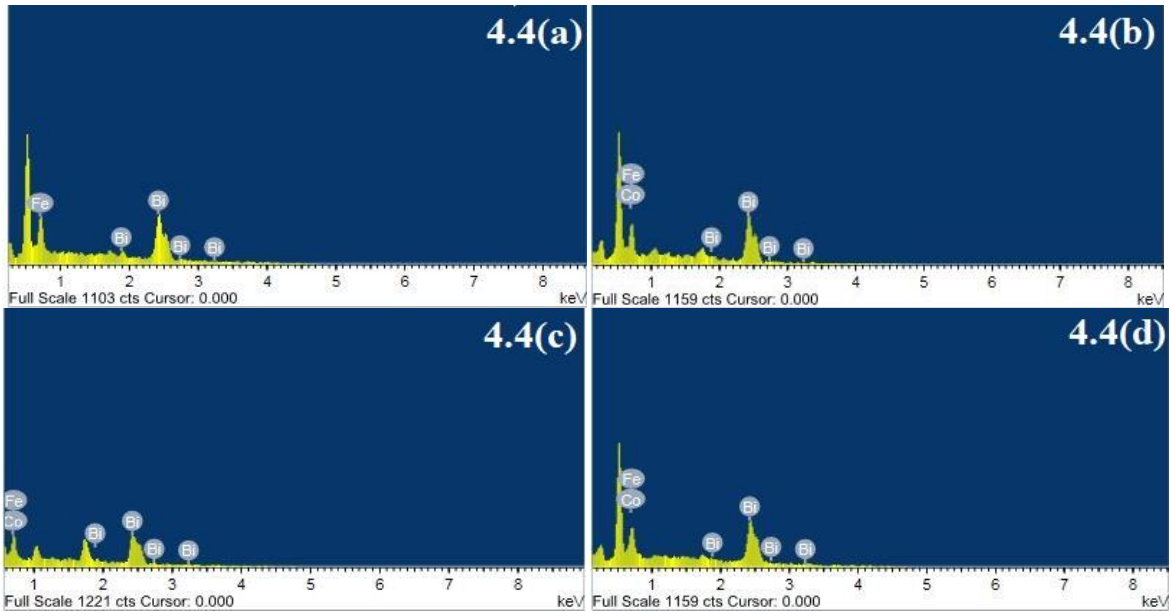

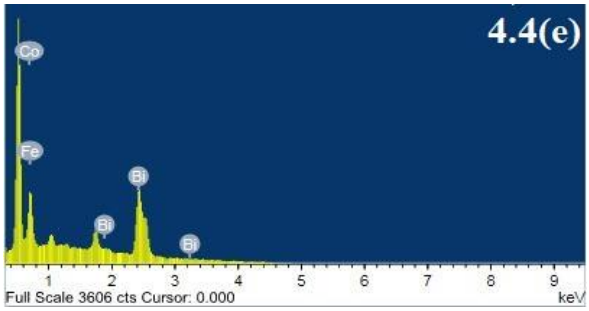

Fig. 4.4 (a-e): (a) x=0, (b) x=0.02, (c) x=0.04, (d) x=0.06 and (e) x=0.08, shows the EDX images of $BiFeO_3$ and $BiFe_{1-x}Co_xO_3$ nanostructured thin films.

Fig. 4.5 shows the FTIR spectra of $BiFeO_3$ and $BiFe_{1-x}Co_xO_3$ nanostructured thin films. The analysis of the FTIR spectra of the metal-oxide band at 400-600 cm^{-1} confirms that the grown samples have a perovskite structure. The FTIR peaks at about 842 cm^{-1} represent the existence of nitrate ions.

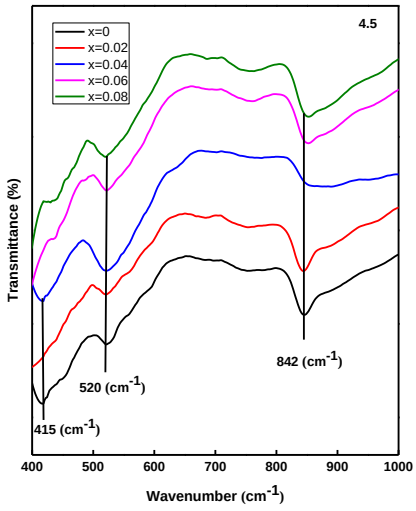

Fig. 4.5: FTIR spectra of $BiFeO_3$ and $BiFe_{1-x}Co_xO_3$ nanostructured thin films.

The UV–Visible spectra of the synthesized $BiFeO_3$ and $BiFe_{1-x}Co_xO_3$ samples are shown in Fig. 4.6. The bandgap of the grown films was calculated using the Tauc plot of the UV-visible spectra, shown in Fig. 4.7. The bandgap values are found to be decreased compared to undoped $BiFeO_3$ thin film, with $BiFe_{1-x}Co_xO_3$ samples with x= 0, 0.02, 0.04, 0.06, and 0.08 respectively.

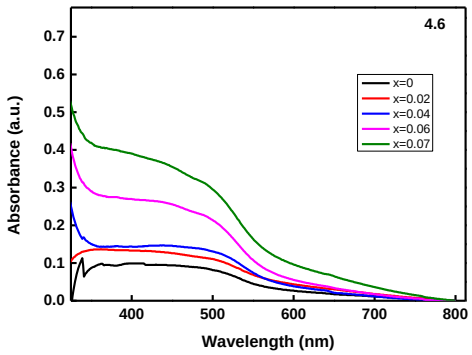

Fig. 4.6: UV–Visible spectra of $BiFe_{1-x}Co_xO_3$ nanostructured thin films.

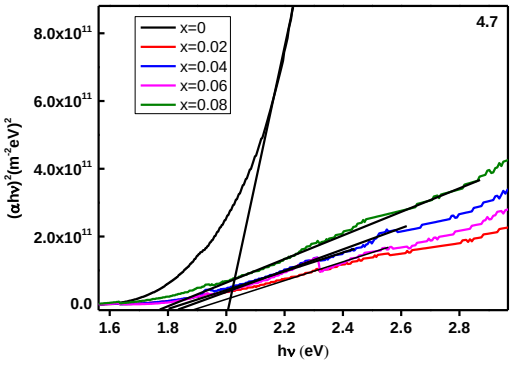

Fig. 4.7: Tauc plot of $BiFe_{1-x}Co_xO_3$ nanostructured thin films.

4.4.3.2 Undoped and Co-Doped BFO Thin Films on p-Si Substrates

Fig. 4.8(a) shows that the XRD spectra of the $BiFeO_3$ and Co-doped $BiFeO_3$ nanostructured thin films show the rhombohedral structure of $BiFeO_3$ with R3c space group. Fig. 4.8(b) shows the enlarged version of the XRD pattern near 2θ=30-34°.

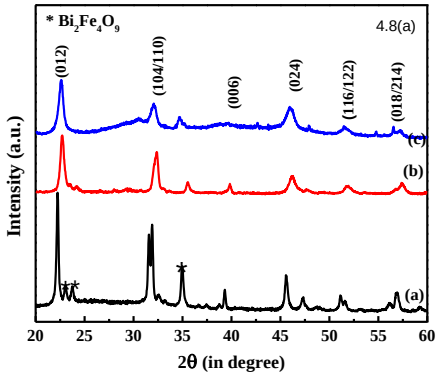

Fig. 4.8(a): XRD patterns of $BiFeO_3$ and $BiFe_{1-x}Co_xO_3$ nanostructured thin films with (a) x=0 (b) x=0.04, and (c) x=0.06.

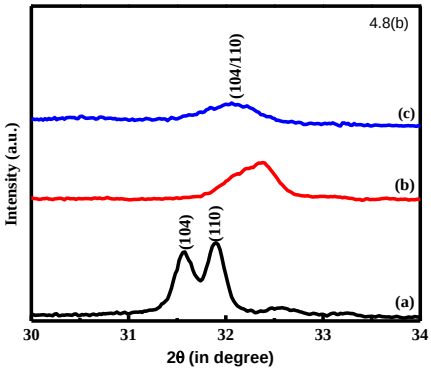

Fig. 4.8(b): magnified XRD patterns in the vicinity of 2θ=32°of $BiFeO_3$ and $BiFe_{1x}Co_xO_3$ nanostructured thin films with (a) x=0 (b) x=0.04, and (c) x=0.06.

Fig. 4.9(a-c) shows the FESEM images of $BiFeO_3$ and $BiFe_{1-x}Co_xO_3$ nanostructured thin films. It was observed that the grain size of $BiFe_{1-x}Co_xO_3$ is significantly smaller than that of the $BiFeO_3$ nanostructured thin films. Co substitution in $BiFeO_3$ helped to obtain higher dense

nanostructured thin films with smaller grain sizes. Fig. 4.10(a-c) shows the EDX spectra of grown nanostructured thin films.

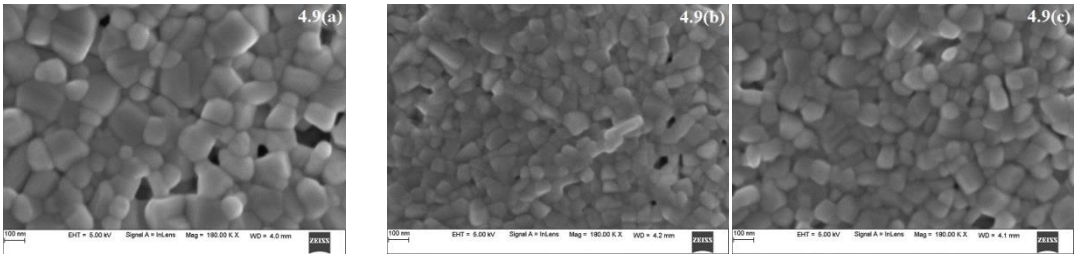

Fig. 4.9(a-c): shows surface morphologies of $BiFe_{1-x}Co_xO_3$ nanostructured thin films with (a) x=0 (b) x=0.04, and (c) x=0.06.

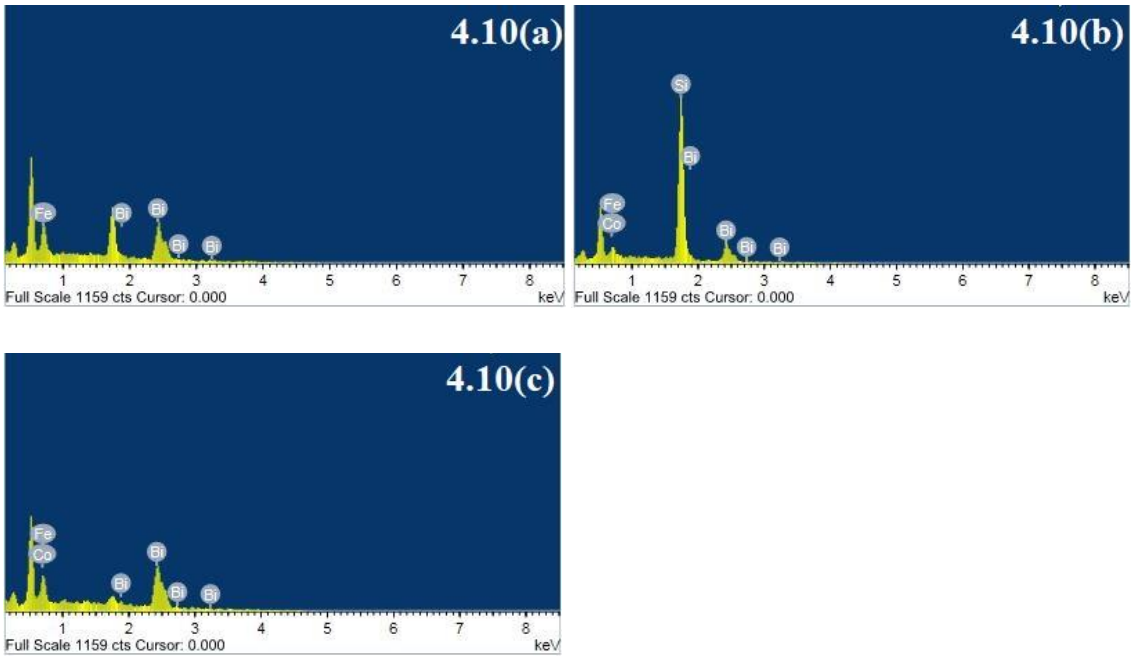

Fig. 4.10(a-c): shows EDX Spectra of $BiFe_{1-x}Co_xO_3$ nanostructured thin films with (a) x=0 (b) x=0.04, and (c) x=0.06.

The average surface roughness of the $BiFeO_3$ and $BiFe_{1-x}Co_xO_3$ nanostructured thin films were measured using AFM images and as shown in Fig.4.11 (a-c). The average surface roughness values were found to decrease with the increase in Co doping. The surface roughness values are 14 nm for $BiFeO_3$ thin film, 12 nm for $BiFe_{1-x}Co_xO_3$ thin film with x=0.04, and 8 nm for $BiFe_{1-x}Co_xO_3$ thin film with x=0.06.

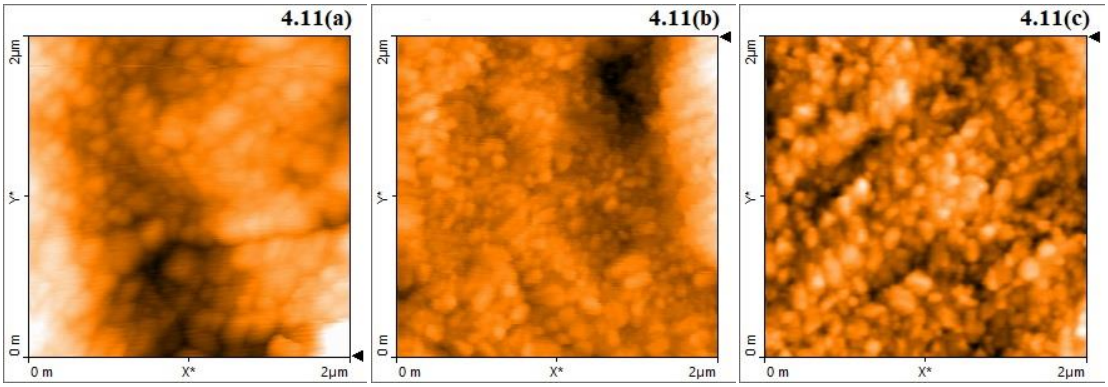

Fig. 4.11(a-c): surface topography images of $BiFe_{1-x}Co_xO_3$ nanostructured thin films with (a) x=0 (b) x=0.04, and (c) x=0.06.

4.5 Chapter-5: Growth and Characterization of Undoped and Dysprosium (Dy)-doped $BiFeO_3$ Thin Films Coated on Glass and p-Si Substrates

This chapter deals with a systematic study of Dy composition-driven structural transformation, optical, and magnetic properties response of $Bi_{(1-x)}Dy_xFeO_3$ for $0 \leq x \leq 0.08$ by using sol-gel spin coating technique. Undoped $BiFeO_3$ and Dy-doped $Bi_{1-x}Dy_xFeO_3$ thin films were deposited on glass and p-Si substrates by the sol-gel spin coating method, followed by a sequential-layer annealing process. Iron nitrate nonahydrate [$Fe(NO_3)_3 \cdot 9H_2O$], bismuth nitrate pentahydrate [$Bi(NO_3)_3 \cdot 5H_2O$], and dysprosium nitrate pentahydrate [$Dy(NO_3)_3 \cdot 5H_2O$] were used as starting materials. 2-methoxyethanol and acetic anhydride in a 3:1 ratio were used as solvents.

4.5.3 Results and Discussion

4.5.3.1 Undoped and Dy-Doped BFO Thin Films on Glass Substrates

Fig. 5.1 shows XRD patterns for the $Bi_{1-x}Dy_xFeO_3$ samples with content of $Bi_{1-x}Dy_xFeO_3$ (x=0, 0.02, 0.04, 0.06, and0.08). The result indicates that the $BiFeO_3$ samples had a distorted perovskite rhombohedral structure and compared them with JCPDS NO 71-2494. Fig. 5.2 shows a magnified pattern around 2θ=30-34°, the evolution of the (104) and (110) twin peaks with Dy doping indicates the structural transition of BFO with the increase in Dy content in $Bi_{1-x}Dy_xFeO_3$ thin films.

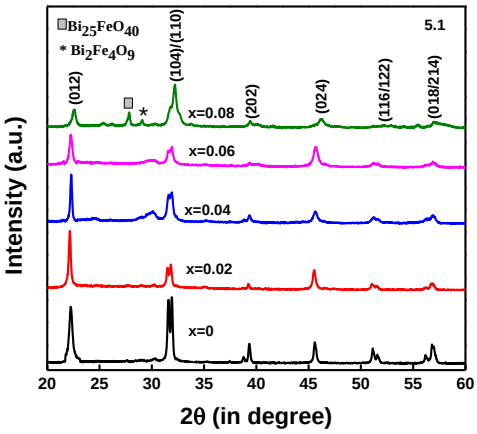

Fig. 5.1: XRD patterns of $Bi_{1-x}Dy_xFeO_3$ nanostructured thin films.

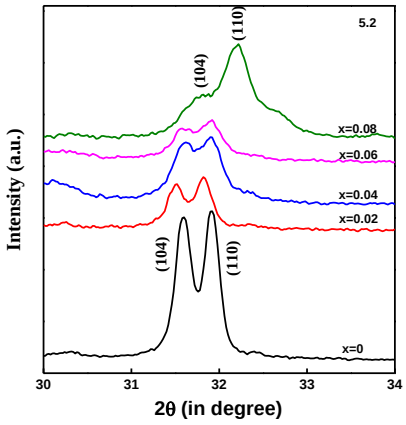

Fig. 5.2: Magnified XRD patterns in the vicinity of 2θ=30-34°.

The surface morphologies of the pure $BiFeO_3$ and $Bi_{1-x}Dy_xFeO_3$ thin films are shown in Fig. 5.3(a–e). A decrease in nanocrystalline particle size was observed with an increase in Dy content in the films. Fig. 5.4 shows the cross-sectional image of $Bi_{1-x}Dy_xFeO_3$ nanostructured thin film.

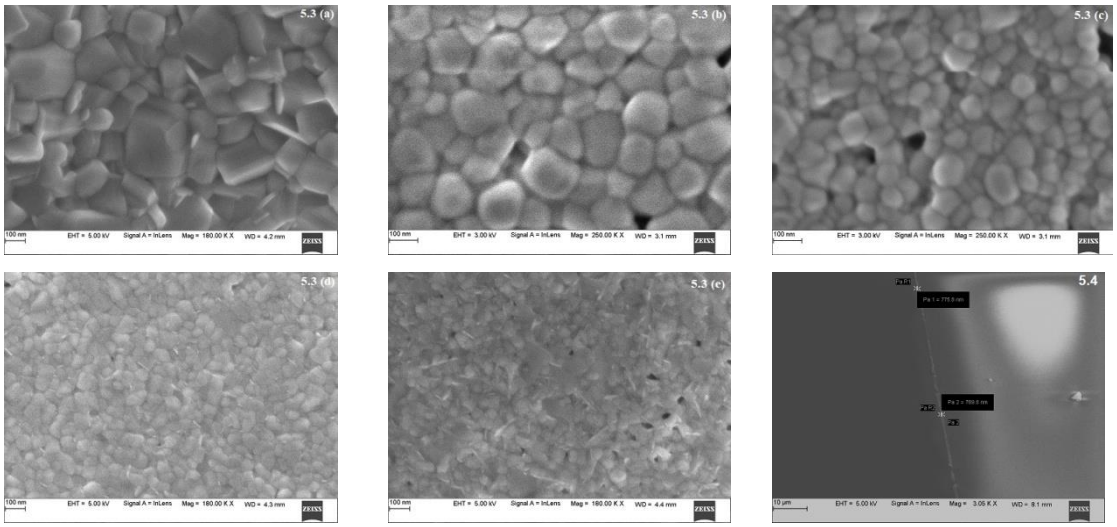

Fig. 5.3(a–e)**:** FESEM images of $Bi_{1-x}Dy_xFeO_3$ nanostructured thin films with (a) x=0 (b) x=0.02 (c) x=0.04, (d) x=0.06 and (e) x=0.08.

Fig. 5.4: The cross-sectional image of $Bi_{1-x}Dy_xFeO_3$ nanostructured thin film.

AFM measurements have measured $Bi_{1-x}Dy_xFeO_3$ surface morphology at various substitution concentrations as shown in Fig 5.5(a-e). The decrease in roughness with a partial fulfillment of dopants can be attributed to an increment in the formation of the BFO phase formations which makes the films structurally granular.

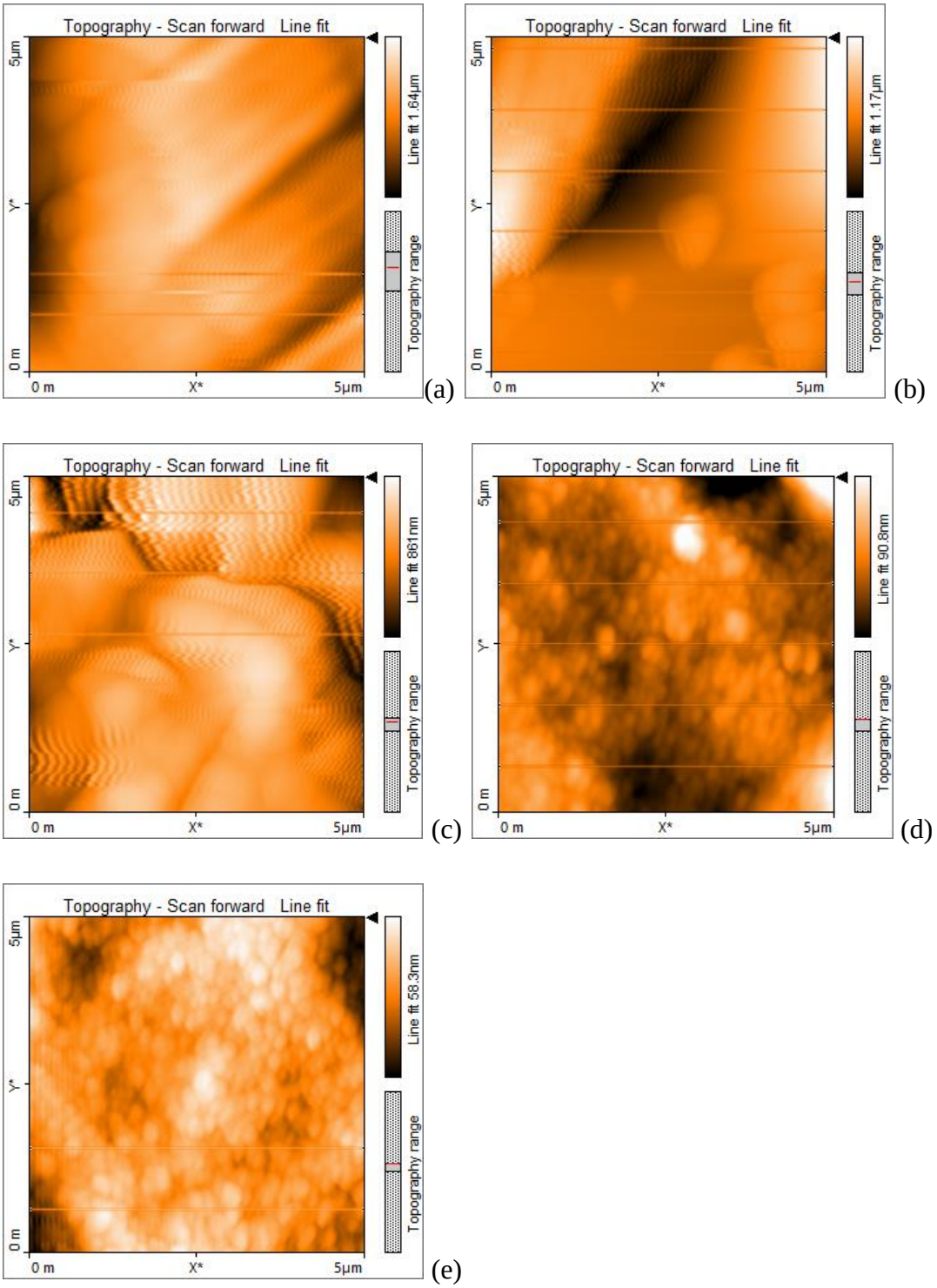

Fig. 5.5(a-e): AFM images of $Bi_{1-x}Dy_xFeO_3$ nanostructured thin films with (a) x=0 (b) x=0.02 (c) x=0.04, (d) x=0.06 and (e) x=0.08.

The UV-visible absorption spectra of the $Bi_{1-x}Dy_xFeO_3$ nanostructured thin films as shown in Fig. 5.6. Figure 5.6(a-e) shows the optical bandgap (E_g) of the undoped $BiFeO_3$ and Dy-doped $BiFeO_3$ samples evaluated by UV–vis absorbance spectroscopy at wavelengths from

200 nm to 800 nm. The optical bandgap of the $BiFeO_3$ and x=0.02, x=0.04, x=0.06, and x=0.08 Dy_x-doped $BiFe_{1-x}O_3$ was 2.14, 2.10, 2.07, 1.88 and 1.87eV, respectively.

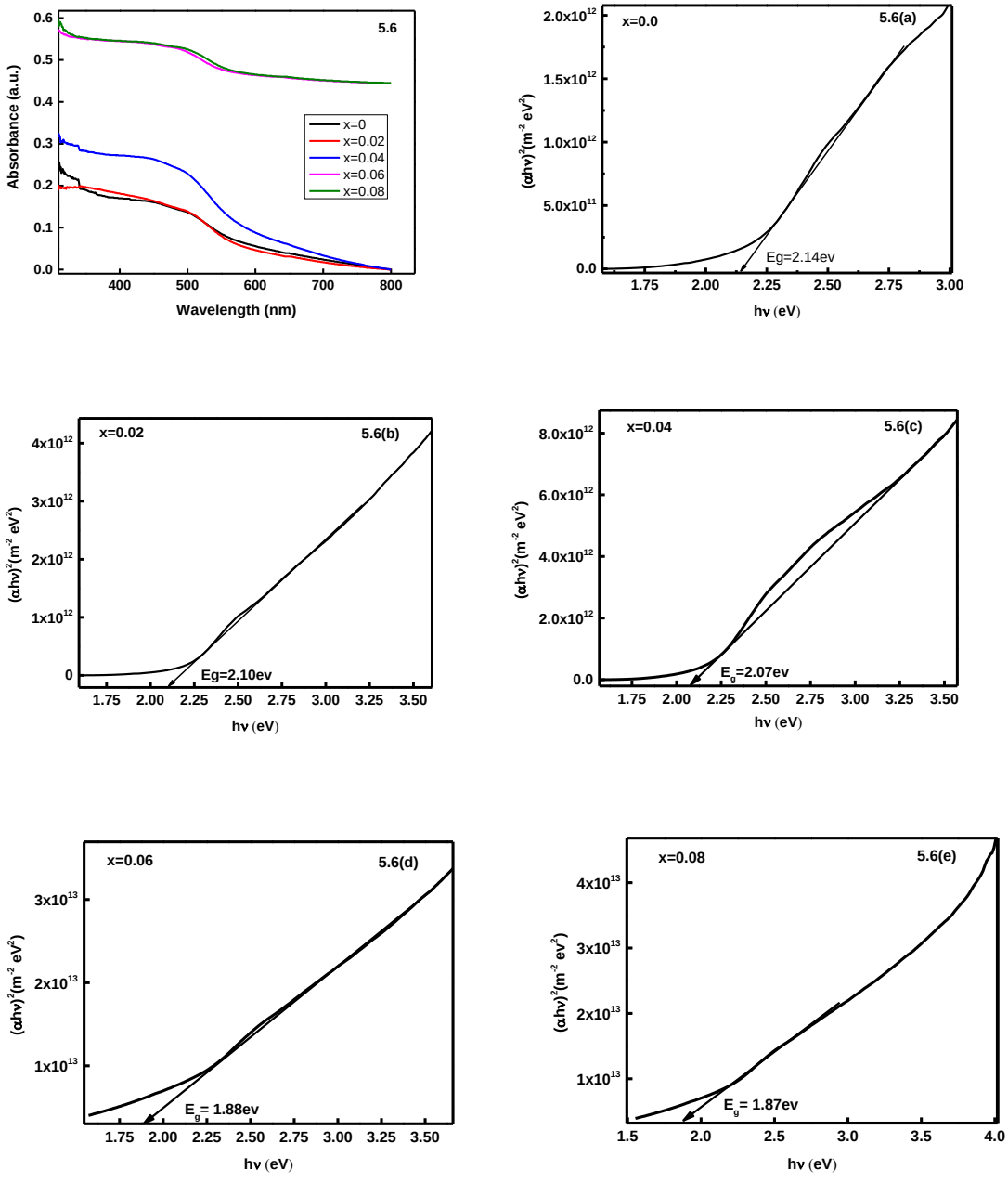

Fig. 5.6: UV-visible absorption spectra of the $Bi_{1-x}Dy_xFeO_3$ nanostructured thin films with (a) x=0 (b) x=0.02 (c) x=0.04, (d) x=0.06 and (e) x=0.08.

Fig. 5.6(a-e): Tauc plot of $Bi_{1-x}Dy_xFeO_3$ nanostructured thin films.

The FTIR measurement was performed in a scan range of 400-1000 cm^{-1} as shown in Fig. 5.7. The characteristic vibration of the octahedral FeO_6 complex group which is assigned to Fe–O stretching and bending vibration is observed in the form of strong absorption peaks near 510 cm^{-1} and 442 cm^{-1}, respectively; implying the formation of the BFO phase.

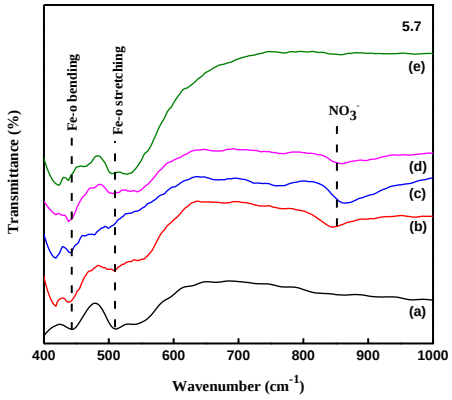

Fig. 5.7: FTIR spectra $Bi_{1-x}Dy_xFeO_3$ nanostructured thin films.

The M-H curves of pure and Dy-doped $BiFeO_3$ thin films show superparamagnetic behavior at 10 K, shown in Fig. 5.8 -5.12. This may be due to the very small, below 50 nm, size of the nanostructured thin film particles. Room temperature M-H curves show ferromagnetic nature in all the measured samples.

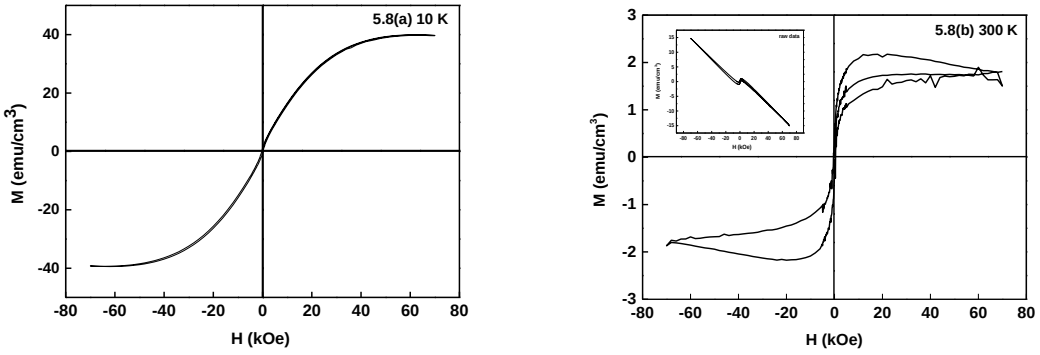

Fig. 5.8(a) and (b): Low and room-temperature M-H hysteresis loops of BFO thin film with x=0.

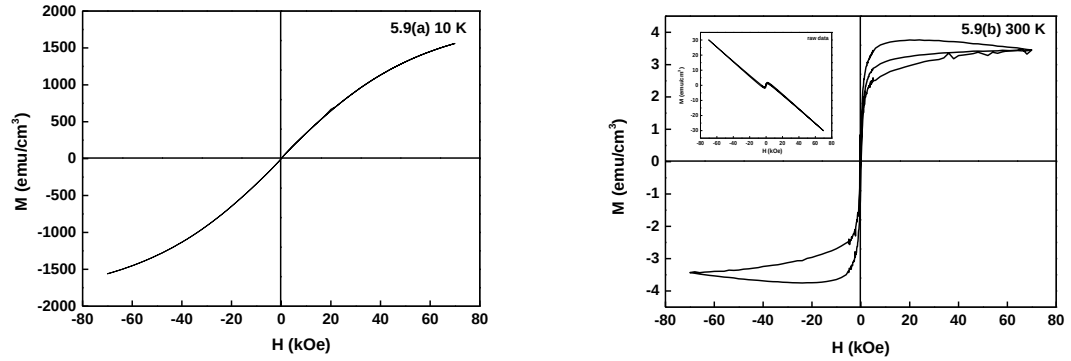

Fig. 5.9(a) and (b): Low and room-temperature M-H hysteresis loops of BFO thin film with x=0.02.

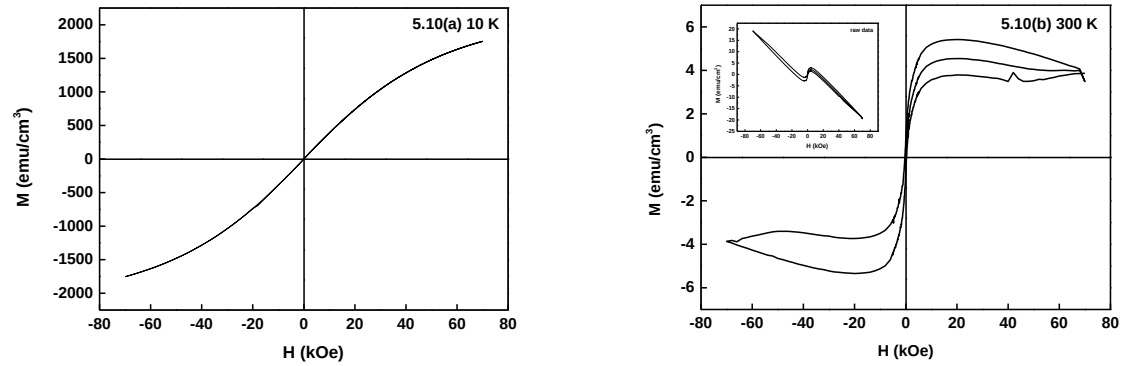

Fig. 5.10(a) and (b): Low and room-temperature M-H hysteresis loops of BFO thin film with x=0.04.

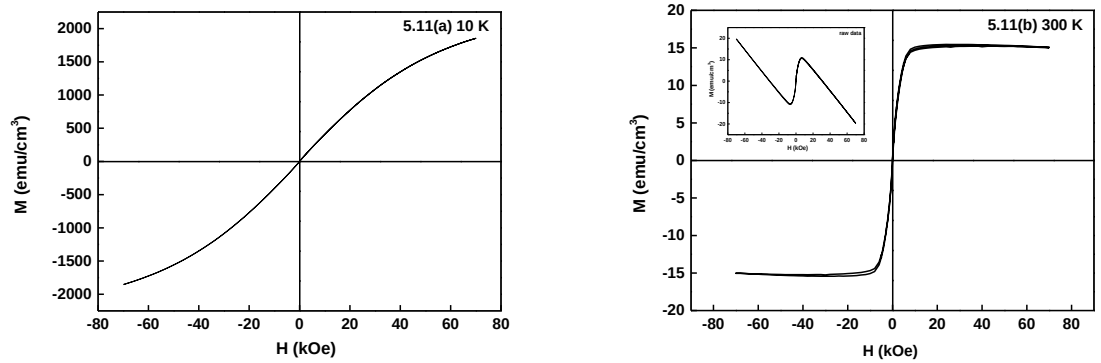

Fig. 5.11(a) and (b): Low and room-temperature M-H hysteresis loops of BFO thin film with x=0.06.

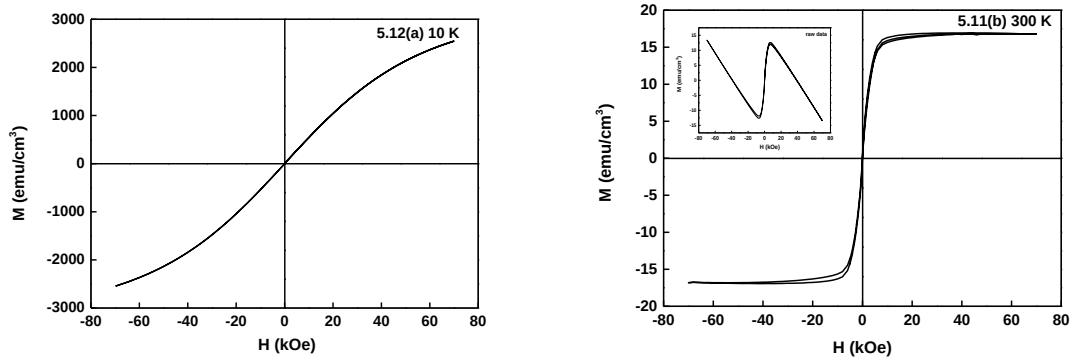

Fig. 5.12(a) and (b): Low and room-temperature M-H hysteresis loops of BFO thin film with x=0.08.

4.5.3.2 Undoped and Dy-Doped BFO Thin Films on p-Si Substrates

Undoped bismuth ferrite ($BiFeO_3$) and Dysprosium doped $BiFeO_3$ ($Bi_{1-x}Dy_xFeO_3$) nanostructured thin films were grown on p-silicon substrates by sol-gel spin coating method with a sequence of coating and annealing process. The post-annealing of the grown films was carried out under a high purity argon atmosphere.

XRD patterns of BFO and $Bi_{1-x}Dy_xFeO_3$ compounds shown in Fig. 5.13(a) depicts that all the compounds crystallize in the rhombohedral structure and the diffraction peaks are indexed with the R3c space group. Along with the main phase BFO, a trace amount of secondary phases like $Bi_2Fe_4O_9$ is observed which is unavoidable during the kinetics of formation of BFO. The magnified XRD patterns in the vicinity of 2θ=30-33° of $Bi_{1-x}Dy_xFeO_3$ nanostructured thin films as shown in Fig. 5.13(b). The morphological features of $BiFeO_3$ and $Bi_{1-x}Dy_xFeO_3$ nanostructured thin film samples, and distribution was observed using field emission scanning electron microscopy (FESEM), and as shown in Fig. 5.14(a-d). With increases in Dy^{3+}, the nanoparticles become smaller, and the shape becomes more and more irregular.

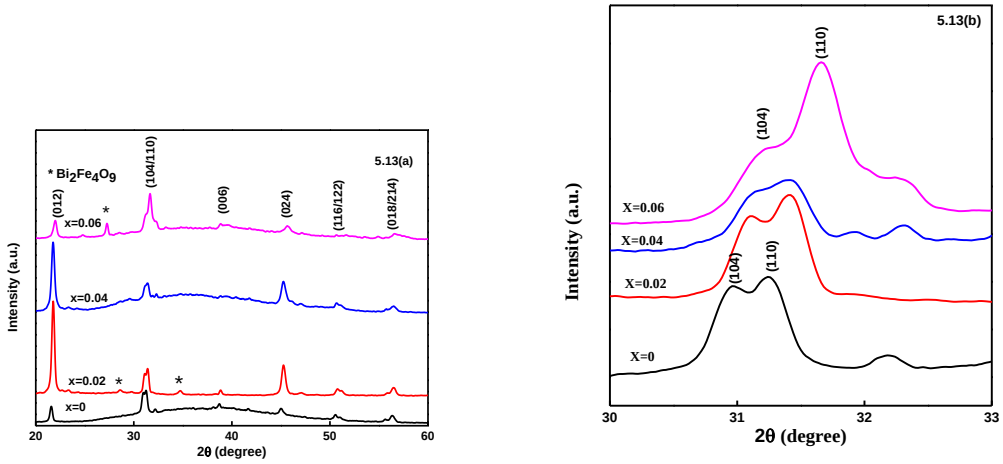

Fig. 5.13(a): XRD patterns of $Bi_{1-x}Dy_xFeO_3$ nanostructured thin films, and **5.13(b):** magnified XRD patterns in the vicinity of 2θ=30-33°of $Bi_{1-x}Dy_xFeO_3$ nanostructured thin films.

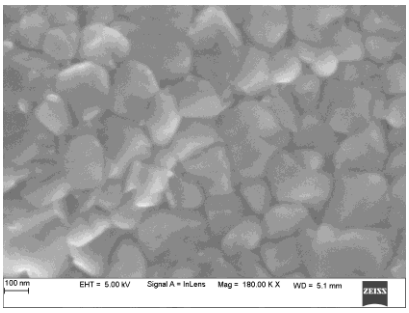
(a)

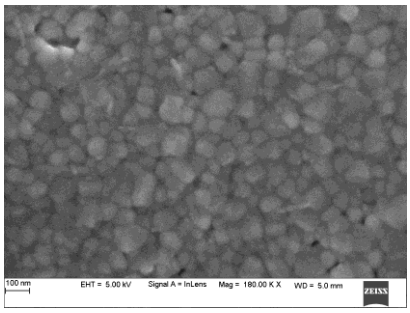
(b)

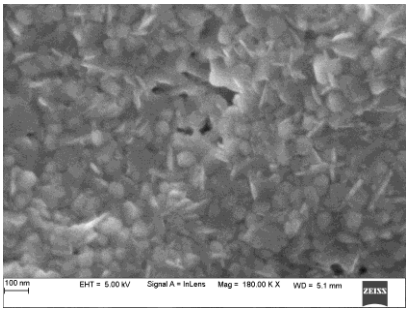
(c)

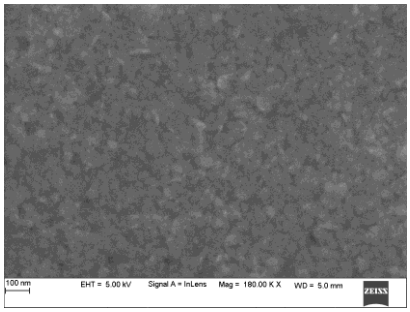
(d)

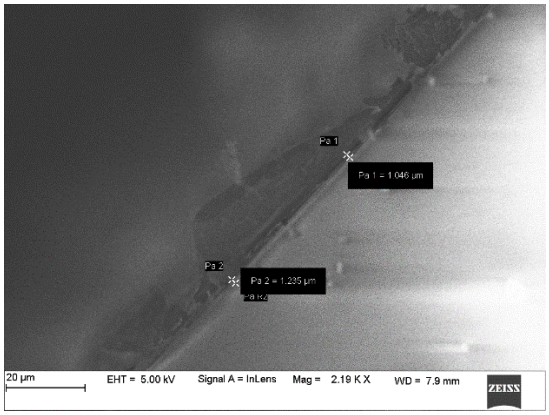

(e)

Fig. 5.14(a-d): surface morphologies of $Bi_{1-x}Dy_xFeO_3$ nanostructured thin films with (a) x=0 (b) x=0.02 (c) x=0.04, and (d) x=0.06. **5.14 (e):** The FESEM cross sectional image of $Bi_{1-x}Dy_xFeO_3$ nanostructured thin film .

The AFM images of $Bi_{1-x}Dy_xFeO_3$ thin films with x=0 to 0.06 are shown in Fig. 5.15(a-d). All films are made from none even crystal grains and the film consist of a small crystal grain in size, with the doping of Dy decreasing its crystal grain size. Moreover, the Dy doping makes the films nearly compact and smooth, which can most likely be responsible for the higher fields used for the measurement of ferroelectricity.

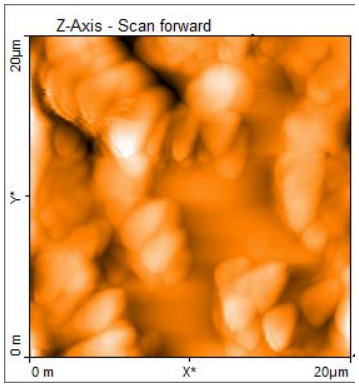

(a)

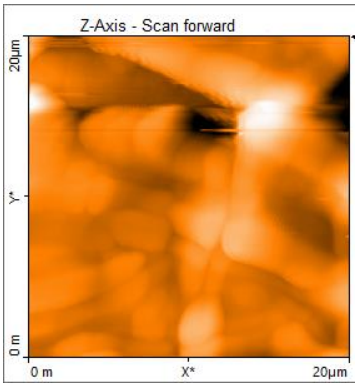

(b)

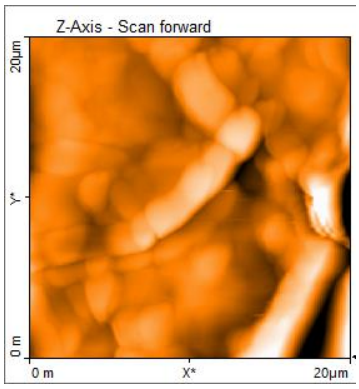

(c)

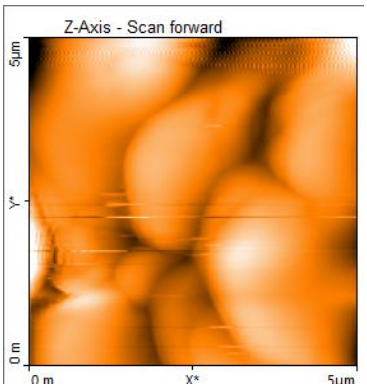

(d)

Fig. 5.15(a-d): shows surface topography of $Bi_{1-x}Dy_xFeO_3$ nanostructured thin films with (a) x=0 (b) x=0.02 (c) x=0.04, and (d) x=0.06.

Fig. 5.16-5.19(a-b) shows the low and room temperature M-H curves of the samples. The 10 K M-H curves show ferromagnetic behavior with very narrow hysteresis loop width for x= 0, 0.02, and 0.04 with decreasing loop with as Dy incorporation was increased from x= 0 to x= 0.4. The 10 K M-H curve for x= 0.06 shows superparamagnetic behavior with a large increase in the saturation magnetization value. The room temperature M-H curves as shown in Fig. 5.16–5.19, the undoped and the Dy doped BFO nanostructured thin films show ferromagnetic behavior.

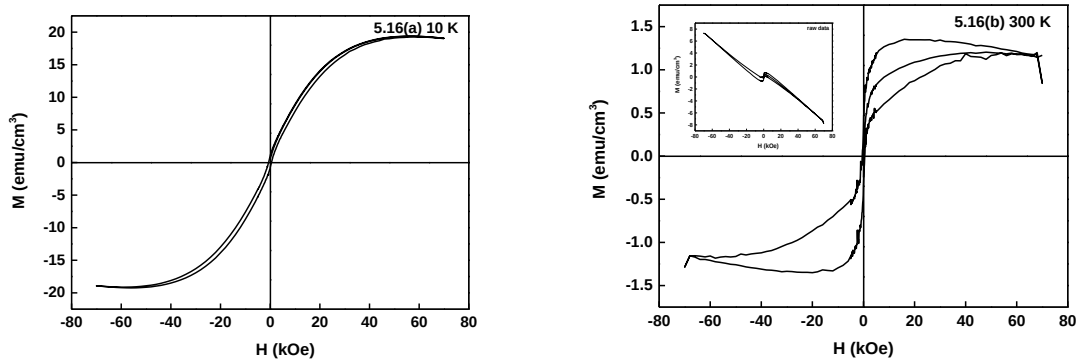

Fig. 5.16(a) and (b): The low and room temperature $Bi_{1-x}Dy_xFeO_3$ magnetic hysteresis loop of nanostructured thin films with x=0.

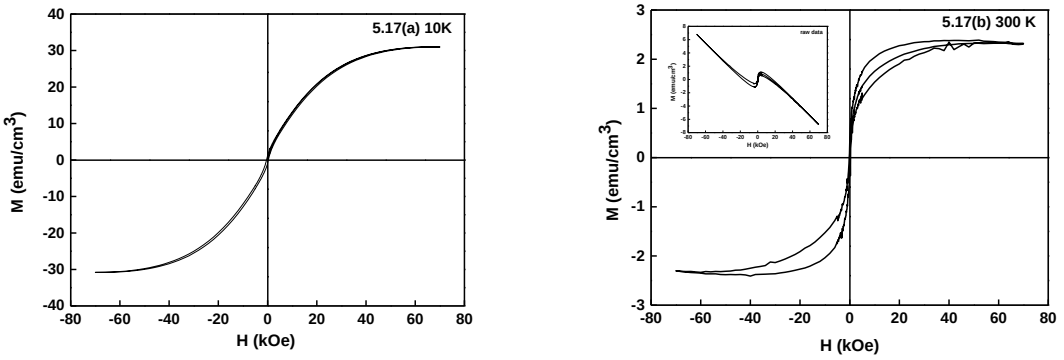

Fig. 5.17(a) and (b): The low and room temperature $Bi_{1-x}Dy_xFeO_3$ magnetic hysteresis loop of nanostructured thin films with x=0.02.

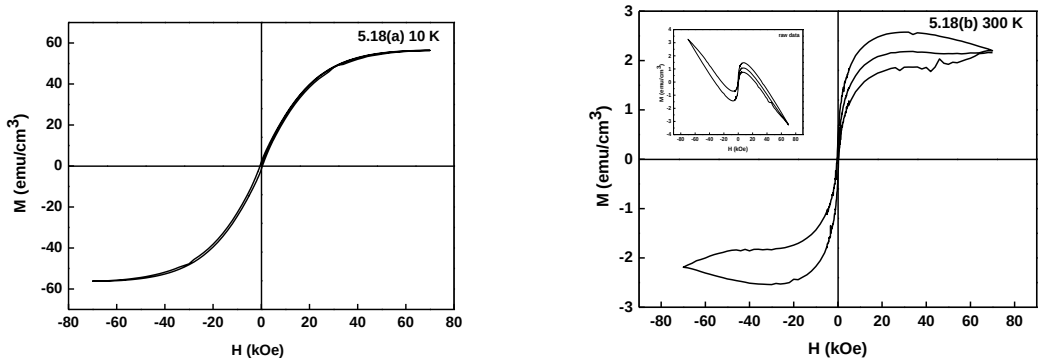

Fig. 5.18(a) and (b): The low and room temperature $Bi_{1-x}Dy_xFeO_3$ magnetic hysteresis loop of nanostructured thin films with x=0.04.

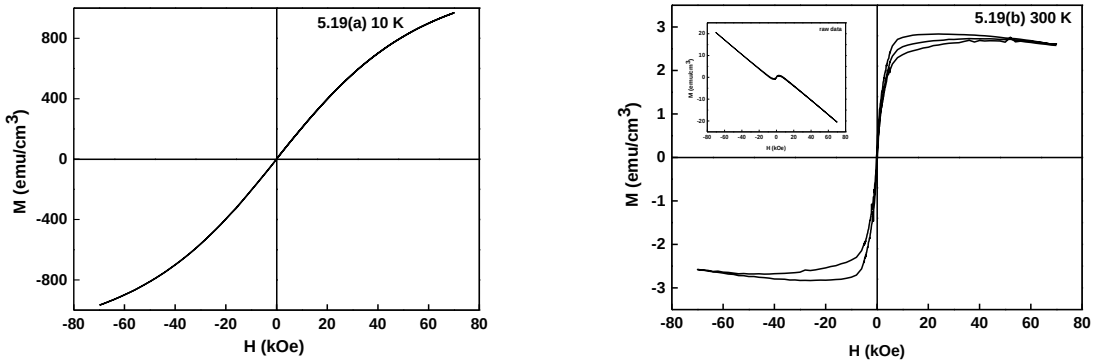

Fig. 5.19(a) and (b): The low and room temperature $Bi_{1-x}Dy_xFeO_3$ magnetic hysteresis loop of nanostructured thin films with x=0.06.

4.6. Chapter 6: Conclusions and scope for future work

4.6.1 Conclusions

Undoped and transition metal ion and rear earth ion doped BFO thin films were deposited on glass and p-Si substrates using sol-gel spin coating method using a sequence of spin coating followed by an annealing process to obtain the desired thickness and crystalline structure of the thin films. The transition elements manganese and cobalt, and rare earth element dysprosium are used as dopants. In all the doped BFO thin films indication of the structural change from distorted rhombohedral to the orthorhombic structure in BFO was observed from powder XRD studies. The FESEM images show nanoparticle size reduction in doped thin films. The AFM studies indicate the decrease in surface roughness with the increase in doping concentration. The optical bandgap measured from the UV-visible

absorption spectrum shows a decrease in bandgap with an increase in doping both in transition metal on doped and rear earth ion doped BFO thin films. The room temperature M-H studies show ferromagnetic behavior in all the samples. The 10 K M-H curves show superparamagnetic behavior in Mn-doped BFO thin films on glass substrates and ferromagnetic behavior in thin films grown on p-Si substrates. The 10 K M-H curves for Dy doped on glass show superparamagnetic behavior and on p-Si shows weak ferromagnetism for low Dy content.

4.6.2 Scope for future work

A more systematic study on the sol-gel synthesis of BFO thin films with both transitions metal and rear earth metal ions is required in terms of their structural, optical, and M-H studies may be very required to gain further understanding of the properties of these thin films in substrates like bare glass, bare silicon as well as in other substrates.

REFERENCES

[1] Hill N. A., and Filippetti A., *"Why are there any magnetic ferroelectrics"*, J. Magn. Magn. Mater., vol. **242**, pp. 976-9, 2002.

[2] Gajek M., Bibes M., Fusil S. Bouzehouane K., Fontcubert J., Barthelemy A., and Fert A.,*"Tunnel junctions with multiferroic barriers"*, Nature Mater., vol. **6**, pp. 296-302, 2007.

[3] Eerenstein W., Mathur N. D., and Scott J. F., *"Multiferroic and magneto-electric materials"*, Nature, vol. **442**, pp. 759-65, 2006.

[4] Seehra M. S., and Helmick R. E., *"Dielectric anomaly in MnO near the magnetic phase transition"*, Phys. Rev. B, vol. **24**, pp. 5098-5, 1981.

[5] Seehra M. S., and Helmick R. E., *"Anomalous changes in the dielectric constants of MnF_2 near its Neel temperature"*, J. Appl. Phys., vol. **55**, pp. 2330-3, 1984.

[6] Lawes G., Ramirez A. P., Varma C. M., and Subramanian M. A., *"Magnetodielectric effects from spin Fluctuations in isostructural ferromagnetic and antiferromagnetic systems"*, Phys. Rev. Lett., vol. **91**, pp. 257208-4, 2003.

[7] Katsufuji T., and Takagi H., *"Coupling between magnetism and dielectric properties in quantum paraelectric $EuTiO_3$"*, Phys. Rev. B, vol. **64**, pp. 054415-4, 2001.

[8] Scott J. F., *"Mechanisms of dielectric anomalies in $BaMnF_4$"*, Phys. Rev. B, vol. **16**, pp. 2329-4, 1977.

[9] Smolenskii G. A., and Chupis I. E., *"Ferroelectromagnets"*, Sov. Phys. Usp., vol. **25**, pp. 475, 1982.

[10] Schmid H., *"Multi-ferroicmagnetoelectrics"*, Ferroelectrics, vol. **162**, pp. 317-338, 1994.

[11] Fox D. L., Tilley D. R., Scott J. F., and Guggenheim H. J., *"Magnetoelectric phenomena in $BaMnF_4$ and $BaMn_{0.99}Co_{0.01}F_4$"*, Phys. Rev. B, vol. **21**, pp. 2926-30, 1980.

[12] Kiselev S. V., Ozerov R. P., and Zhdanov G. S., *"Detection of magnetic Order in ferroelectric $BiFeO_3$ by Neutron Diffraction"*, Sov. Phys. Dokl., vol. **7**, pp. 742, 1963.

[13] Teague J. R., Gerson R., and James W. J., *"Dielectric hysteresis in single crystal $BiFeO_3$"*, Solid State Commun., vol. **8**, pp. 1073-4, 1970.

[14] Michel C., Moreau J. M., Achenbach G. D., Gerson R., and James W. J., *"The atomic structure of $BiFeO_3$"*, Solid State Commun., vol. **7**, pp. 701-4, 1969.

[15] Kubel F., and Schmid H., *"Structure of a ferroelectric and ferroelastic monodomain crystal of the perovskite $BiFeO_3$"*, Acta Crystallogr. Sect. B, vol. **46**, pp. 698-702, 1990.

[16] Dzyaloshinskii I. E., *"Thermodynamic theory of weak ferromagnetism in antiferromagnetic substances"*, Sov. Phys. JETP, vol. **5**, pp. 1259-1272, 1957.

[17] Moriya T., *"Anisotropic Superexchange Interaction and Weak Ferromagnetism"*, Phys. Rev. B, vol. **120**, pp. 91-8, 1960.

[18] Sosnowska I., Neumaier T. P., and Streichele E., *"Spiral magnetic ordering in bismuth ferrite"*, J. Phys. Chem. C, vol. **15**, pp. 4835-46, 1982.

[19] Popov Y. F., Kadomtseva A. M., Zvezdin A. K., *"Magnetoelectronic Phenomena in Crystals"*, Edited by Manfred Fiebig, Kluwer Academic, Boston, 2004.

[20] Anwara, Z., Khana, M. A., Mahmood, A., Asghar, M., Shakir, I., Shahid, M., Bibi, I., and Warsi, M. F., *"$Tb_xBi_{1-x}FeO_3$ nanoparticulate multiferroics fabricated by micro-emulsion technique: Structural elucidation and magnetic behavior evaluation"*, *J. Magn. Magn. Mater*., vol. **355**, pp. 169-172, 2014.

[21] Soram, B. S., Ngangom, B. S., and Sharma, H. B., *"Effect of annealing temperatures on the structural and optical properties of sol-gel processed nanocrystalline $BiFeO_3$ thin films"*, *Thin Solid Films,* vol. **524**, pp. 57-61, 2012.

[22] Ahad. F. B. A., Hung, D. S., Yao, Y. D., Lee, S. F., Tu, C. S., Wang, T. H., Chen, Y. Y., and Fu, Y. P., *"Dielectric constant at x-band microwave frequencies for multiferroic $BiFeO_3$ thin films"*, *J. Appl. Phys.*, vol. **105**, pp. 07D912, 2009.

[23] Pattanayak, S, Choudhary, R. N. P., and Das, P. R., *"Studies of electrical conductivity and magnetic properties of $Bi_{1-x}Gd_xFeO_3$ multiferroics"*, *J. Adv. Dielectr*., vol. **4**, no. 2, pp. 1450011, 2014.

[24] Ramesh, R., and Spanldin N. A., *"Multiferroics: progress and prospects in thin films, Nat. Mater"*, vol. **6**, 2007.

[25] Ali, S., Kiani, M., and Rizwan, *"Structural, Magnetic and Dielectric Properties of $Sm^{3+}$and Mn^{2+} Co-doped $BiFeO_3$ Nanoparticles"*, *J. Min. Metall. B*., vol. **6**, pp. 1000163, 2017.

[26] Ghosh, A. K., Dwivedi, G. D., Chatterjee, B., Rana, B., Barman, A., Chatterjee, S., and Yang, H. D., *"Role of codoping on multiferroic properties at room temperature in $BiFeO_3$ ceramic"*, *Solid State Commun*., vol. **166**, pp. 22-6, 2013.

[27] Batttisha, I. K., Farag, I. S. A., Kamal, M., Ahmed, M. A., Girgis, E., Meleegi, H. A. E., and Desouki, F. E., *"Dielectric and Magnetic Properties of Nano-Structure $BiFeO_3$*

Doped with Different Concentrations of Co Ions Prepared by Sol-Gel Method", New Journal of Glass and Ceramics., vol. **5**, pp. 59-73, 2015.

[28] Tang, P., Kuang, D., Yang, S., and Zhang, Y., *"The structural optical and enhanced magnetic properties of $Bi_{1-x}Gd_xFe_{1-y}Mn_yO_3$ nanoparticles synthesized by sol-gel", J. Alloys Compd*., vol. **622**, pp. 194-9, 2015.

[29] Makhdoom, A. R., Akhtar, M. J., Rafiq, M. A., Siddique, M., Iqbal, M., and Hasan, M. M., *"Enhancement in the multiferroic properties of $BiFeO_3$ by charge compensated aliovalent substitution of Ba and Nb", AIP Adv*., vol. **4**, 037113, 2014.

[30] Priyadharsini, P., Pradeep, A., Sathymoorthy, B., and Chandrashekaran, G., *"Enhanced multiferroic properties in La and Ce co-doped $BiFeO_3$ nanoparticles", J. Phys. Chem. Solids*, vol. **75**, pp. 797-802, 2014.

[31] Sharma, H. B., Singh, Ng. B., Devi, K. N., Lee, J. H., and Singh, S. B., *"Structural and optical properties of manganese substituted nanocrystalline bismuth ferrite thin films by sol-gel process", J. Alloys Compd*., vol. **583**, pp. 106-10, 2014.

[32] Song, G. L., Su, J., Ma, G. J., Wang, T. X., Yang, H. G., and Chang, F. G., *"Effects of trivalent gadolinium and cobalt co-substitution on the crystal structure, electronic transport, and ferromagnetic properties of bismuth ferrite", Mater. Sci. Semicond. Process*., vol. **27**, pp. 899-908, 2014.

LIST OF PUBLICATIONS

1. **R. Prasannakumara**, and K. Gopalakrishna Naik, '*Structural and optical properties of cobalt doped multiferroics $BiFeO_3$ nanostructured thin films',* **AIP Conf. Proc.,** 1953, 030106, 2018, DOI: 10.1063/1.5032441.
2. **R. Prasannakumara**, B. V. Shrisha, and K. Gopalakrishna Naik, '*Synthesis of cobalt doped $BiFeO_3$ multiferroic thin films on a p-Si substrate by sol-gel method',* **AIP Conf. Proc.,** 1953, 030247, 2018, DOI: 10.1063/1.5032582.
3. **R. Prasannakumara**, D. P. Rai, and K. Gopalakrishna Naik, '*Study of optical and magnetic properties of Mn substituted bismuth ferrite thin films',* **J. Mate. Sci.: Mater. Electron.,** vol **32**, pp. 28542-28552, 2021, DOI.org/10.1007/s10854-021-07233-2.

Papers Presented in Conferences

1.**R.Prasannakumara**, B. V. Shrisha, Shashidhara Bhat, and Dr.K. Gopalakrishna Naik K,18th International Workshop on Physics of Semiconductor Devices (IWPSD-2015), **(poster presentation),** "Sol-gel synthesis and characterization of pure and Mn-doped $BiFeO_3$thinfilms", Indian Institute of Science (IISc), Bangalore, 7-10th Dec 2015.

2. **R.Prasannakumara**, B. V. Shrisha, Shashidhara Bhat, D. Sathish, M. Parvathi Venu, and Dr.K. Gopalakrishna Naik, International Conference on Nanoscience, Nanotechnology and Advanced Materials (NANOS2015), **(Oral Presentation),** "Growth and Characterization of Mn-doped Bismuth ferrite thin films by Sol-Gel method", GITAM University, Visakhapatnam, 14-17th Dec 2015.

3. **R. Prasannakumara** and Dr.K. Gopalakrishna Naik, Conference on Emerging Materials (CEMAT-2016), **(Poster Presentation),** "Ar annealed cobalt doped $BiFeO_3$ nanostructured thin films", IISc, Bangalore, 18-19thJuly 2016.

4. **R.Prasannakumara,** B. V. Shrisha, Shashidhara Bhat, and Dr.K.Gopalakrishna Naik, National Conference on Particle Accelerators in Interdisciplinary Research (PAIR), **(oral presentation),** "Transition element Manganese doped multiferroic Bismuth Ferrite thin films", Dept. of studies in Physics, Mangalore University, Mangalore, 11-13 April 2017.

Signature of Research Scholar Signature of Research Guide

(Prasannakumara R.) (Dr. K. Gopalakrishna Naik)